Molecular Therapy
Nucleic Acids
Original Article

Control of endothelial cell function and arteriogenesis by MEG3:EZH2 epigenetic regulation of integrin expression

Hywel Dunn-Davies,[2,7] Tatiana Dudnakova,[1,7] Antonella Nogara,[1] Julie Rodor,[1] Anita C. Thomas,[3] Elisa Parish,[1] Philippe Gautier,[4] Alison Meynert,[4] Igor Ulitsky,[5] Paolo Madeddu,[3] Andrea Caporali,[1] Andrew Baker,[1] David Tollervey,[2] and Tijana Mitić[1,6]

[1]University/British Heart Foundation Centre for Cardiovascular Science, Queen's Medical Research Institute (QMRI), The University of Edinburgh, 47 Little France Crescent, Edinburgh EH16 4TJ, UK; [2]Wellcome Centre for Cell Biology, University of Edinburgh, Michael Swann Building Max Born Crescent, King's Buildings, Edinburgh EH9 3BF, UK; [3]Bristol Medical School, Translational Health Sciences, University of Bristol, Research and Teaching Floor Level 7, Queens Building, Bristol Royal Infirmary, Bristol BS2 8HW, UK; [4]MRC Human Genetics Unit, MRC Institute of Genetics and Cancer, The University of Edinburgh, Western General Hospital, Crewe Road, Edinburgh EH4 2XU, UK; [5]Department of Immunology and Regenerative Biology and Department of Molecular Neuroscience, Weizmann-UK Building rm. 007, Weizmann Institute of Science Rehovot 76100, Israel

Epigenetic processes involving long non-coding RNAs regulate endothelial gene expression. However, the underlying regulatory mechanisms causing endothelial dysfunction remain to be elucidated. Enhancer of zeste homolog 2 (EZH2) is an important rheostat of histone H3K27 trimethylation (H3K27me3) that represses endothelial targets, but EZH2 RNA binding capacity and EZH2:RNA functional interactions have not been explored in post-ischemic angiogenesis. We used formaldehyde/UV-assisted crosslinking ligation and sequencing of hybrids and identified a new role for maternally expressed gene 3 (MEG3). MEG3 formed the predominant RNA:RNA hybrid structures in endothelial cells. Moreover, MEG3:EZH2 assists recruitment onto chromatin. By EZH2-chromatin immunoprecipitation, following MEG3 depletion, we demonstrated that MEG3 controls recruitment of EZH2/H3K27me3 onto integrin subunit alpha4 (*ITGA4*) promoter. Both MEG3 knockdown or EZH2 inhibition (A-395) promoted *ITGA4* expression and improved endothelial cell migration and adhesion to fibronectin *in vitro*. The A-395 inhibitor re-directed *MEG3*-assisted chromatin remodeling, offering a direct therapeutic benefit by increasing endothelial function and resilience. This approach subsequently increased the expression of *ITGA4* in arterioles following ischemic injury in mice, thus promoting arteriogenesis. Our findings show a context-specific role for *MEG3* in guiding EZH2 to repress *ITGA4*. Novel therapeutic strategies could antagonize MEG3:EZH2 interaction for pre-clinical studies.

INTRODUCTION

The vascular endothelium is essential for maintaining cardiovascular homeostasis during health and disease. Cytoskeletal rearrangements are critical for endothelial cell (EC) morphogenesis in response to endothelial injury during atherosclerosis or other cardiovascular disease (CVD). In response to such injury, multiple extracellular matrix proteins and cell surface ligands act to alter endothelial function at an intercellular level.[1]

Many non-coding RNAs (ncRNAs) are involved in directing the signaling pathways behind endothelial dysfunction, with implications for CVD,[2] but complete mechanisms require further research. Long ncRNAs (lncRNAs) are an added level of epigenetic regulation of target genes ensuing recruitment of chromatin remodeling complexes. With their regulatory functions in *cis* and in *trans* at the transcriptional and post-transcriptional levels, the lncRNAs can affect physiological and pathological processes responsible for CVDs, such as ischemic heart disease.[3,4] Several nucleus-localizing lncRNAs have been reported to interact with the enhancer zeste homolog 2 (EZH2), and the enzymatic component of the transcriptional corepressor, polycomb repressive complex 2 (PRC2)[5] that writes histone H3 lysine K27 tri-methylation (H3K27me3) mark.[6] EZH2 is a well-recognized epigenetic regulator of cardiovascular development and diseases.[7] The removal of H3K27me3 through PRC2 inhibition increases recovery after limb ischemia[8] and improves aortic performance in a model of thoracic aortic aneurysm[9] or in disease states known to arise from endothelial dysfunction.[10] Despite the large body of research evidence detailing the lncRNA-driven mechanisms

Received 15 November 2022; accepted 14 March 2024;
https://doi.org/10.1016/j.omtn.2024.102173.

[6]Present address: Centre for Cardiovascular Science, The University of Edinburgh Queen's Medical Research Institute (QMRI), Edinburgh BioQuarter, 47 Little France Crescent, Edinburgh EH16 4TJ, Scotland, UK

[7]These authors contributed equally

Correspondence: Dr. Tijana Mitić, University/British Heart Foundation Centre for Cardiovascular Science, Queen's Medical Research Institute (QMRI), The University of Edinburgh, 47 Little France Crescent, Edinburgh EH16 4TJ, UK.
E-mail: tijana.mitic@ed.ac.uk

in endothelial dysfunction, new risk factors continue to be unraveled involving the EZH2 cell-specific actions and intricate function in cardiovascular remodeling, hypoxia, apoptosis, and endothelial to mesenchymal transition.[11,12]

The large nuclear retained lncRNA maternally expressed gene 3 (MEG3) associates with chromatin.[13] MEG3 antagonizes angiogenesis, as increased vascularization is observed in the MEG3 knockout embryos, further suggesting that inhibition of MEG3 is pro-angiogenic.[14,15] Increased MEG3 expression is seen in primary ECs, and this is both age dependent and hypoxia induced (e.g., during ischemia) leading to pulmonary hypertension.[16,17] Moreover, MEG3 depletion improved angiogenic responses following femoral artery ligation (limb ischemia) in aged mice and attenuated endoplasmic reticulum stress-mediated apoptosis following myocardial infarction, leading to blood flow recovery.[18] Despite seemingly a valid target to improve post-ischemic angiogenesis, the role of MEG3 in chromatin remodeling of endothelial dysfunction has not been assessed. We postulated that this could involve context-specific regulation of MEG3-guided EZH2 deposition or structure-based interactions.[13]

In this study, we first aimed to explore EZH2:RNA functional interaction in primary ECs to test the RNA binding capacity of EZH2 relative to its ability to capture the RNA-RNA interactions (hybrid reads); adding to its prevailing chromatin binding capacity. The study specifically addressed EZH2 direct interaction with MEG3 in primary ECs. As we identified that EZH2 targets MEG3:MEG3 secondary structures we asked if pro-angiogenic lncRNA-MEG3 is directly involved in guiding EZH2 and depositing H3K27me3 methylation onto the regulatory region of endothelial genes. We next aimed to unveil how they repress vascular gene expression leading to endothelial dysfunction, which can block the initiative event during ischemia-induced angiogenesis. Ultimately, we aimed to explore EZH2 as a potential therapeutic target to help restore endothelial function and to promote arteriogenesis in ischemic pathologies.

RESULTS

EZH2-FLASH identifies direct endothelial RNA targets

Our experimental approach is outlined in Figure 1A. To generate the endothelial EZH2-RNA interactome, we performed formaldehyde and UV crosslinking assisted ligation and sequencing of hybrids (FLASH) in primary ECs as a robust method to identify direct protein-RNA interactions[19–21] (Figure 1B). By immunoprecipitation against EZH2, total protein bound RNA was isolated and ligated, followed by deep sequencing and data analysis to obtain and identify (1) direct RNA targets (single reads) and (2) RNA-RNA interactions (hybrid reads) associated with EZH2 protein. Statistically significant differences were identified in >15,000 peaks (N1, 15,399; and N2, 16,768). Significant differentially expressed (DE) EZH2-FLASH targets, with RNA gene classification, i.e., biotypes ($log_2FC > 0.5$) are given in Table S1.

The 30% of single FLASH reads mapped within intronic and intergenic regions represented as "other RNA" (Figure 1B) and indicating that *bona fide* interactions were recovered. Our data are consistent with prior reports of EZH2 preferentially targeting nascent transcripts.[22] We identified a total of 390 ($log_2FC > 0.5$) novel lncRNAs and found known lncRNA targets. Among the top 20 represented lncRNAs bound to EZH2, the *MEG3* (Ensembl: ENSG00000214548.14) was recovered (Table S1; Figure S1A) with single and multiple hybrid hits detected in both replicates (Tables S2 and S3, respectively). Resultant sequences of EZH2 single hits have been validated and aligned with MEG3 gene sequence (Pairwise Sequence Alignment; https://www.ebi.ac.uk/Tools/msa/clustalo/).[23] Focusing on MEG3-lncRNA, high EZH2 binding was found over exons regions of MEG3 RNA, supporting functional interactions (∼75% over MEG3 exons 3–7 and 25% on introns) (Figure S1B). More than one annotated transcript was derived from the MEG3 genomic region, with most EZH2 reads distributed over ENST00000451743.6 (RefSeq: NR_002766.2, transcript variant 1) relative to the ENST00000423456.5 (RefSeq:NR_003530, transcript variant 2; Figure S1C), as per Ensembl release 77.[24] The MEG3 ENST00000451743.6 transcript is already known to be highly expressed in aorta and tibial artery according to GTEx profile (GTEx: https://gtexportal.org/home/transcriptPage). In a separate RNA immunoprecipitation (RIP) experiment when we precipitated the repressive chromatin (EZH2 and H3K27me3 mark, see Materials and methods) using UV-crosslinked lysates of ECs, a maximum recovery is observed over exon 3 of MEG3, against which region the primers were designed (Figure S1D). There was minimal binding observed in the same region of exon 3 for other PRC2 subunits, SUZ12 and EED, and none for the JARID2 co-factor. Motif analysis using MEME identified enriched sequence motifs within MEG3 fragments associated with EZH2 (Figure 1D). These motifs comprised "XTCAC" and "AGGX" nucleotides.

EZH2 targets structures within MEG3 in ECs

The RNA-RNA duplexes associated with EZH2 as chimeric cDNA species were identified by FLASH (biological replicates; 3,944 hybrids from N1 and 3,228 hybrids from N2), revealing the predominance of MEG3:MEG3 base pairing over MEG3 base pairing with other RNAs (Figure 1E). The specific MEG3:MEG3 base pairing sites were also identified in the replicate datasets (Figure S1E) and are representative of MEG3 intermolecular secondary structure. The overlay of EZH2 hybrid sites with the EZH2-FLASH single hits over MEG3 (Figures S1A and S1E) signifies that EZH2 binding is constrained to the MEG3 structures. It was preferentially associated with the exon 3 of *MEG3* transcripts (Figures S1B and S1C). Hybrids counts were plotted against the predicted binding energy of MEG3 interactions for EZH2-FLASH (i) and IgG-FLASH (ii) (Figure S1F, i and ii). MEG3:MEG3 interactions found in chimeras were the dominant ones captured by EZH2-FLASH as seen in Figure 1F and most interactions were between MEG3 positions 52,623–52,670, corresponding to highly conserved exon 3, and some in positions 75,277–76,613. The computational analysis pipeline used with the FLASH is given in Figure S2. Total counts were mapped for genomic features of all annotated hybrids and are represented with their position along the MEG3 genomic sequence. "*Viennad*" files for clustering of

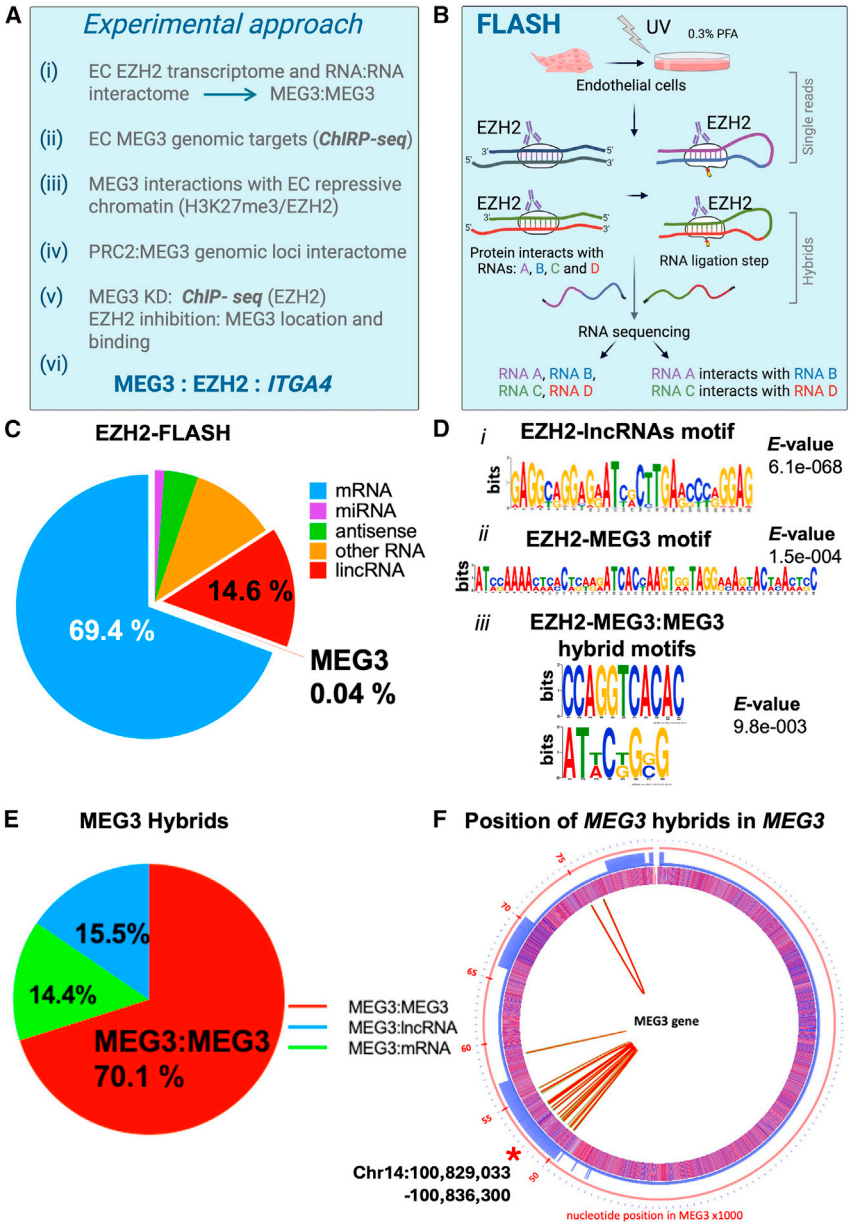

Figure 1. EZH2-FLASH identifies direct endothelial RNA targets

(A) Experimental approach used in the study with plan and listed experiments. (B) Schematic representation of steps in FLASH (formaldehyde and UV crosslinking, ligation, and sequencing of hybrids) with EZH2 immunoprecipitation using lysates from UV crosslinked HUVECs. Dynamic EZH2:RNA complex formation occurs as represented. Following RNA ligation and hybrid formation between interacting RNAs, sequencing is performed. Further analysis of single and hybrid reads bound by EZH2, reveals interacting RNA molecules. (C) Distribution of annotated reads over genome, with gene classification (biotype), from statistically filtered EZH2-FLASH data with two biological replicates in HUVECs and MEG3-lncRNA (0.04%, red line) as the lncRNA candidate (14.6%, red wedge). (D) (*i* and *ii*) Enriched motifs with sequences in *MEG3* mRNA of EZH2-FLASH that uniquely overlap exons; the logos were drawn using the top 4–8 nt K-mers for each experimental replicate (*top* and *middle*) and *Z*-score for each. Motif analysis was performed using the MEME suite.[58] (*iii*) Enriched motif within the fragments of MEG3:MEG3 hybrids. (E) Total RNA-RNA interactions associated with MEG3 at chr14:100, 829,033-100,836,300 (Hg38), (MEG3 id = NR_002766.2) and distribution of all MEG3 interactions among various classes of RNAs as captured by EZH2-FLASH. (F) Intermolecular MEG3-RNA interactions captured by EZH2-FLASH. Hybrid counts were mapped for all annotated hybrids' genomic features, and those of MEG3 were plotted in the Circos plot, aligning with their position along the MEG3 genomic sequence. The main MEG3 hybrid detected is MEG3, that is represented by the number of interactions in red. Red circle shows the position within the MEG3 gene in kilobases with *50–55 kb falling within exon 3. The blue circle is a visual representation of MEG3 exons. Regions overlapping exons are represented in solid blue. The purple broad circle shows the nucleotides at each position: (A) dark blue, (B) light blue, (T) light red, (G) dark red. The inner part of the white circle shows MEG3:MEG3 hybrids; arcs connecting the center of each hybrid fragment are shown in red, and the regions spanned by the hybrid fragments are shown in light green.

MEG3:MEG3 interactions (hybrids), identifying the interacting nucleotides, are given in Table S3, with *dG* energy of folding predictions showing most convincing base pairings.

We asked what are the changes that come with EZH2 binding MEG3 in ECs and we set to explore the role of MEG3:EZH2-mediated gene regulation on EC function. Given that EZH2 recognizes the repressive mark H3K27me3, we reasoned that the distribution of this histone modification over the gene body of all MEG3 potential targets in ECs could be brought about via MEG3:EZH2 interaction. Therefore, we next investigated the MEG3 genomic targets in ECs and identified common MEG3/EZH2 direct targets on which MEG3 could guide PRC2 activity.

MEG3 directly targets angiogenic genes

To unravel chromatin-associated MEG3 interactions and functions in primary human umbilical vein endothelial cells (HUVECs), we identified MEG3-genomic binding sites. Using chromatin isolation by RNA purification (ChIRP) we obtained DNA targets. Chromatin was isolated after glutaraldehyde crosslinking of ECs, followed by RNA purification for qPCR, and DNA purification for sequencing. Biotinylated antisense probes were designed and used against *MEG3*

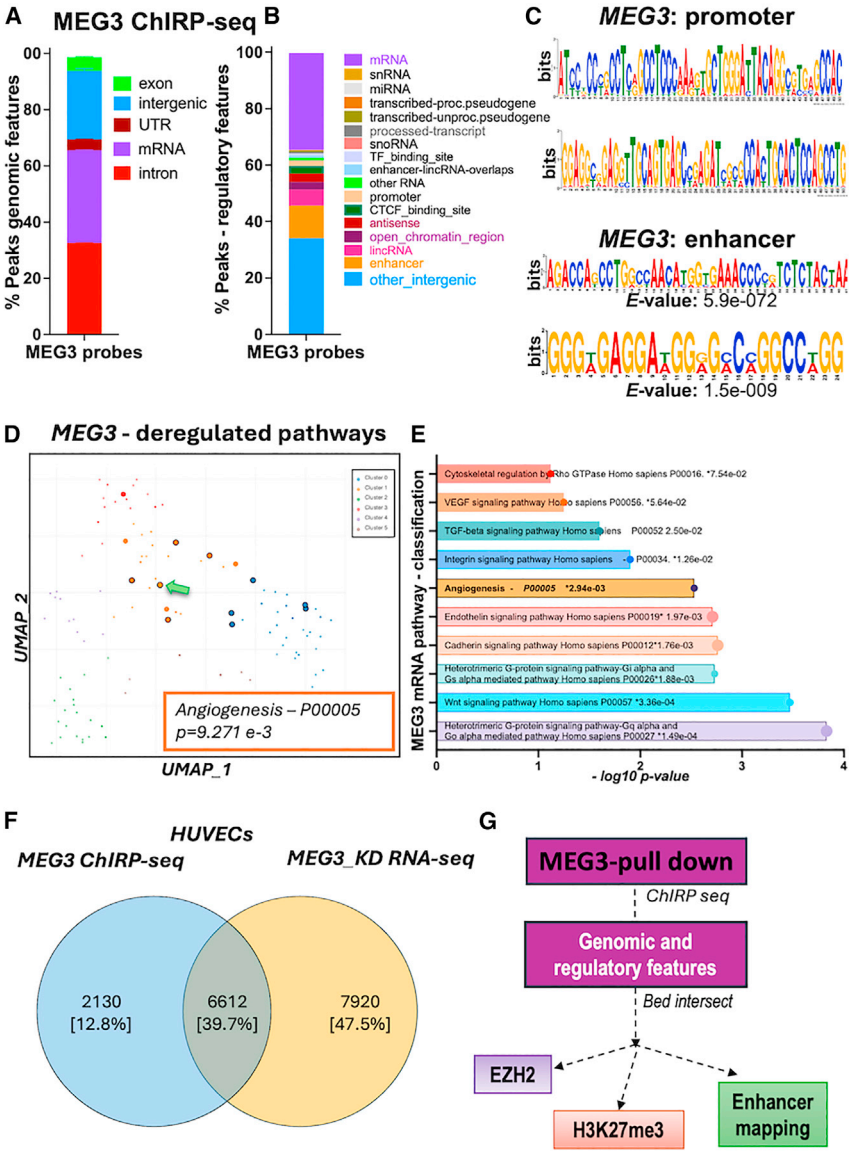

Figure 2. MEG3 directly targets angiogenic genes

(A) ChIRP-seq analysis showing percent of peak elements in the genomic features upon MEG3-ChIRP pull-down using biotinylated probes against the MEG3 gene to isolate associated DNA for sequencing and RNA for qPCR validation of probes (Figure S3C). The ChIRP pull-down with LacZ oligos was used as negative control. n=2 biological replicates with odd and even probes against MEG3 was followed by bioinformatics analysis to merge the individual replicates and boost the signals. (B) ChIRP-seq as in (A) with a display of percent peaks over named regulatory elements. (C) Enriched motifs with sequences in *MEG3* mRNA of ChIRP-seq peaks that uniquely overlap promoter, enhancer, TF, open chromatin, and CTCF binding region were assessed (see supplemental information); logos were drawn using the top 50 nt K-mers for each experimental replicate and a *Z* score was calculated for each. Top enriched motifs by E value (statistical significance as calculated by MEME) within the (i) promoter sequence and (ii) enhancer binding, that uniquely overlapped regions associated with MEG3 probes. Motif analysis was performed using the MEME suite[58] and all motifs are listed in the supplemental information. (D) Volcano plot of gene enrichment analysis for all MEG3 ChIRP peak-associated genes (left) with top-rated GO biological pathway annotations (right). EnrichR analysis with Panther Pathway resource was used to associate most represented genes with pathways[78] and p value was calculated by the Binomial statistic with a cutoff of 0.05 used as a start point. (E) MEG3-associated pathways with p values, classified using Panther Pathway analysis for MEG3-ChIRP-seq mRNAs targets. (F) Overlap between MEG3 mRNA targets obtained from ChIRP-seq experiments and RNA-seq of *MEG3* KD performed in HUVECs (shown in Figures 3E and S5; Table S7). (G) Overview of the critical steps to obtain MEG3-bound genomic loci and intersections with EZH2 and H3K27me3 ChIP signals (GEO databases for HUVECs). The intersection between GEO EZH2 ChIP, GEO H3K27me3 ChIP, and statistically filtered MEG3-ChIRP data from two biological replicates was performed. Overlapping features were mapped and enhancer regions exposed. The number of genes and degree of overlap is obtained between MEG3- and PRC2-dependent genes. The p values are a result of hypergeometric test.

or *LacZ* control (Figure S3A). MEG3 probes specifically recognized Ensembl: ENST00000451743.6 and Ensembl: ENST00000423456.5 transcripts and not GAPDH (Figures S3B and S3C). MEG3 ChIRP-seq identified >9,000 peaks associated with genomic (Figure 2A) and regulatory features (Figure 2B) in HUVECs. Genomic loci were associated with the intergenic and intronic regions of the genes, and a small proportion were in exon, promoter, and enhancer regions. Motif enrichment analysis of regulatory sequences, revealed top conserved DNA sequence patterns of MEG3 recognizing the promoter regions (Figure 2C, i) comprising "GCCTCCC" and "CCAACA" nucleotides. These sequences were also observed within the MEG3 enhancer binding motif (Figure 2C, ii) and within some gene promoters (see supplemental information). The computational analysis pipeline used for ChIRP-seq data processing is outlined in Figure S3D. As a result, we obtained 9,822 and 7,490 loci as MEG3-binding peaks from two independent experiments (n=2), which respectively associated with annotated regions and genes (Table S4). The function of these MEG3-associated genes was assigned using EnrichR classifications (Figure 2D) and Panther pathway analysis (Figure 3E) and we identified pathways with direct relevance to endothelial repair, with gene ontology (GO) biological processes terms related to cell adhesion (EBI: GO:0007155) and angiogenesis (EBI: GO:0001525).[25] The occupancy was seen on multiple genes belonging to Wnt signaling (Wnt, β-catenin), cadherin signaling (*CDH1* and *CDH3*), integrin (*ITGA3*, *ITGA4*), VEGF, and TGF-β signaling, all related to the

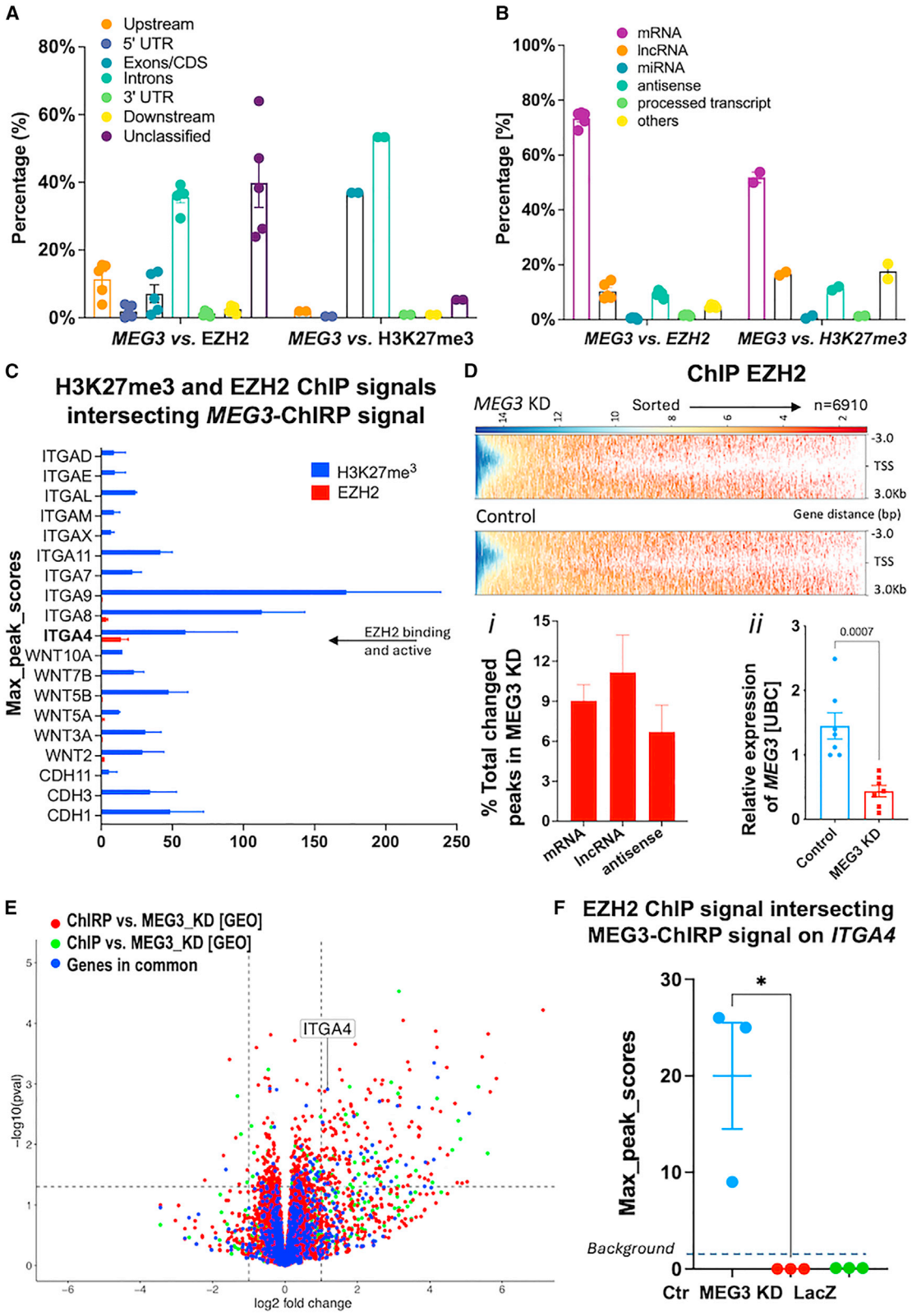

(legend on next page)

process of angiogenesis GO:0001525. The qPCR validation of top MEG3-genomic targets was performed in separate ChIRP experiments, with signal enrichment over selected targets being shown in Figure S3E. Among the MEG3 targets, we also found the genomic locus of *EZH2* (chr7:148,806,055–148,900,311), signifying MEG3 physical interaction with *EZH2* gene (Figure S3F).

To further validate direct MEG3 targets MEG3-ChIRP-seq was intersected with the transcriptional profile of HUVECs depleted of MEG3 (Figure 2F). *MEG3* knockdown (KD) resulted in transcriptional upregulation (Table S7); with nearly 40% of targets also detected by ChIRP-seq, suggesting that they are sites of direct regulation by MEG3.[26] The pathway analysis of the overlapping genes is displayed in Figure S5A.

Overlap between MEG3 genomic targets sites with *EC* chromatin occupancy by EZH2 and H3K27me3

To study the relationship between MEG3-regulated targets and EZH2-chromatin binding sites in human ECs, we overlaid the datasets. Bioinformatics bed intersection of MEG3 ChIRP-seq with published EZH2 and H3K27me3 chromatin immunoprecipitation sequencing (ChIP-seq) data (Figure 2G) was performed. As the enrichment profile of H3K27me3 can depend on the cellular context, we systematically analyzed the genome-wide profile of H3K27me3 tracks from the Gene Expression Omnibus (GEO) (via ncbi.nlm.nih.gov) datasets of ChIP-seq performed in HUVECs. The following datasets were found, for EZH2 ChIP under accession number GSE109626, GSM733688, and GSM945180 for H3K27me3 ChIP. MEG3-ChIRP-seq peaks that overlapped with ChIP-seq peaks for EZH2/H3K27me3 chromatin occupancy were obtained. The distribution of overlapping peaks was plotted in relation to the gene region (Figure 3A) and biotype (Figure 3B). All overlapping genes are given in Table S6 and functional profiling of genes with maximum peak scores is given in Table 1. Computational analysis with pipeline is given in Figure S4A. Many overlapping peaks fell within the intronic regions of the genes, suggesting that MEG3 and EZH2 bind nascent transcripts and together promote PRC2 protein complex assembly.[27] In addition to the gene body, overlapping signals were observed upstream of the transcription start site (TSS) in ∼15% of promoter regions (Figure 3A, orange), i.e., at active genes and locations already enriched in H3K27me3 chromatin modification[22] (Table S6). The convergence of EZH2 and H3K27me3 peaks was seen in over 40% of intronic regions, and for >60% mRNA (Figure 3B). We hypothesized that the genomic occupancy of MEG3/PRC2 is higher for their mutually regulated direct targets. Top MEG3 peaks, enriched in both EZH2 and H3K27me3 ChIP signals (from publicly available GEO datasets), were identified and we obtained the maximum peak score for each gene (Figure 3C). Significant EZH2/H3K27me3 occupancy of MEG3-ChIRP targets hints at the possible existence of distinctive features for a group of MEG3-regulated genes. We identified enrichment of genes involved in the processes of integrin, cadherin, and Wnt-signaling and confirmed their overlap between MEG3 and EZH2 occupancy, as seen in Figure 3C. As an additional validation of above dependencies, we sought mutually regulated targets by MEG3 and EZH2/PRC2 in primary ECs.

EZH2 landscape in MEG3-deficient ECs

To test the functional importance of MEG3-EZH2 interactions in primary HUVECs, we identified genomic loci with MEG3-dependent EZH2 deposition that could modulate endothelial gene expression. MEG3 was depleted by >70% using GapmeRs (Figure 3D, i and ii, *MEG3* KD) to decipher how it affects EZH2 enrichment or the activity of PRC2 complex. ChIP-seq was then employed to examine global landscape of EZH2 occupancy in control and *MEG3* KD cells. EZH2 enrichment was observed at >6,000 regions in control, associated with a total of 4,785 peaks. Depletion of MEG3 resulted in decreased levels of EZH2 at ∼10% of target regions (Figure 3D, i) and was lost or reduced at a total of ∼563 loci (Table S8). The targeted promoter regions were sorted by EZH2 occupancy in control vs. MEG3-deficient HUVECs, with gene enrichment for common molecular functions and biological pathways represented in Table 2. Reduction or loss in EZH2 signal upon depletion of MEG3 was preferentially seen for genes with GO terms for "biological adhesion" or cell-cell adhesion, and cell junctions; and belonging to integrin, cadherin, and Wnt-signaling pathways in line with gathered evidence. Next, three-way intersection of datasets in HUVECs identified commonly regulated targets and enriched GO terms with relevant pathways (Figure S5B). The volcano plot in Figure 3E shows in red the genes commonly seen between ChIRP-seq experiment (Figure 2) and *MEG3* KD HUVECs; in green are genes commonly seen between ChIP-seq targets

Figure 3. Overlapping targets between MEG3 and repressive chromatin (EZH2 and H3K27me3) in ECs

(A) Convergence of MEG3-ChIRP peaks overlapping EZH2-ChIP peaks or H3K27me3 peaks at genomic loci with the named gene regions. (B) Distribution of MEG3-ChIRP peaks overlapping EZH2-ChIP peaks or H3K27me3 peaks with intersecting reads in relation to gene type. (C) Maximum peak score of ChIP signal for EZH2 and H3K27me3 intersecting the top enriched MEG3 peaks associated with nearest genes. Highest EZH2 peak score is over ITGA4, with H3K27me3 activity also detected in ITGA4, ITGA7, ITGA8, and ITGA9, members of the ITGA family. (D) Heatmap showing distribution of reads from EZH2 ChIP-seq experiment. Signal densities at all unique RefSeq genes within TSSs ±3 kb are sorted by EZH2 occupancy, in control vs. MEG3-deficient (10 nM) HUVECs. (i) Percent total changed representable peaks in *MEG3* KD (mRNA, antisense, and lncRNA genes) from ChIP-seq. (ii) Depletion of MEG3 gene in HUVECs (10 nM LNA GapmeRs) was achieved with MEG3 relative expression showing ∼70% reduction compared with control (Ctr). (E) Volcano plot of differentially expressed genes with log fold change (logFC) on the *x*-axis from *MEG3* KD in HUVECs and the in-house ChIRP-seq (MEG3, human, HUVECs) $-\log10p_{adj}$ on the *y*-axis. Representative co-detected genes (red) between two datasets are statistically significant and represent bona fide MEG3 targets. Among the overlapping targets we highlighted in green the genes commonly seen between the ChIP-seq experiment (Figure 3D) and *MEG3* KD. Finally, in blue are genes from the ChIP-seq experiment (Figure 3D) commonly found between all three datasets *MEG3* KD, ChIP-seq, and ChIRP-seq. We highlighted the *ITGA4* gene that belongs to the angiogenesis pathway and is mutually regulated by MEG3:EZH2. Similar overlap with murine dataset is represented in Figures S6D and S6E. (F) Maximum peak scores of the overlapping signal over the *ITGA4* promoter obtained by intersection of the EZH2 ChIP signal (D) with the MEG3-ChIRP signal (A) at this promoter region (chr2:181,457,035–181,458,302). Upon depletion of MEG3 the EZH2 signal is significantly reduced and there is no overlap with the MEG3 ChIRP signal.

Table 1. Functional profiling of overlapping genes with maximum peak scores between ChIP signal for EZH2 and H3K27me3 vs. MEG3-ChIRP peaks

ID	Source	Term ID	Term name	p_{adj} (query_1)
1	GO:BP	GO:0007155	cell adhesion	6.091×10^{-21}
2	GO:BP	GO:0022610	biological adhesion	1.330×10^{-21}
3	GO:BP	GO:0007267	cell-cell signaling	4.476×10^{-13}
4	GO:BP	GO:0030029	actin filament-based process	3.637×10^{-13}
5	GO:BP	GO:0098609	cell-cell adhesion	1.535×10^{-13}
6	GO:BP	GO:0098742	cell-cell adhesion via plasma membrane adhesion	3.745×10^{-11}
7	GO:BP	GO:0034330	cell junction organization	4.404×10^{-10}
8	GO:BP	GO:0034329	cell junction assembly	1.687×10^{-9}

Genes in common were functionally profiled (left) with named pathways (right) represented for top enriched mRNA targets, as per Figure 3C. Biological pathway regulating cell adhesion was predominant. BP, biological pathways.

(Figure 3D) and *MEG3* KD HUVECs. Finally, in blue are genes from ChIP-seq experiment that are commonly found between all three datasets *MEG3* KD, ChIP-seq, and ChIRP-seq; with *ITGA4* (*integrin subunit alpha 4*) highlighted as top regulated by MEG3:EZH2 among all datasets (Figure 3E). The permutation tests that showed that the set of mRNAs identified in the ChIRP, ChIP, and RNA-seq datasets (which includes *ITGA4*) was found to have a significantly higher log2 fold change than would be expected for a randomly selected set of mRNAs of equivalent size. This effect was seen in both the new HUVEC RNA-seq data ($p = 0.0007644$) and the C2C12 data ($p = 0.02422$; Figure S6D and S6E). We further chose to focus on *ITGA4*, and to validate its regulation in HUVECs as a mutual target of MEG3:EZH2 identified in our approach and of relevance for angiogenesis.

Specifically, at the *ITGA4* locus, binding of EZH2-ChIP was reduced due to MEG3 depletion (Figure 3F). The EZH2 ChIP signal overlaps the MEG3-ChIRP binding at the *ITGA4* locus and it is lost due to MEG3 depletion. This finding suggests that MEG3 regulation of *ITGA4* expression (Figure S5C). In addition a clear dependency and mutual epigenetic landscape by EZH2 and MEG3 in ECs is observed, alongside enrichment of activating histone marks (H3K4me3, H3K27Ac) and other PRC2 components (EED, SUZ12), to directly regulate the *ITGA4* promoter (Figures S8A) suggesting an early acquired bivalent regulation[28]

MEG3 targets EZH2- and H3K27me3-regulated integrin signaling

To dissect MEG3:EZH2-mediated regulation in HUVECs we explored the relationship between MEG3 and PRC2 binding. We next sub-classified the ChIRP-MEG3 targets into groups according to EZH2 occupancy following MEG3 depletion and gene transcription activity in the EZH2-deficient HUVECs vs. control (Figure 4A). We identified differentially regulated genes in EZH2-silenced HUVECs following *de novo* RNA-seq gene expression analysis, alignment, and data mapping to human genome Hg38. *siEZH2* RNA-seq re-derived dataset from HUVECs (GSE71164) is given in Table S7 and Figure S10. To identify targets with a differential PRC2-RNA binding capacity rather than those where PRC2 binds to chromatin, we created genome-wide datasets. The set of 418 genes (blue and pink overlap) represents the EZH2 deregulated RNA interactome, not bound at DNA level, but exemplifies a novel unconventional function of EZH2 to bind RNA targets, specifically in line with the cytoplasmic distribution of EZH2.[29] Based on their nature of interaction with PRC2 and MEG3, we sub-classified genes into two types of targets: group 1, MEG3-dependent EZH2 target genes at the DNA level (175 genes) and group 2, at the RNA level (205 genes). In *group 1*, MEG3-PRC2 DNA targets are the genes with EZH2 deposition (ChIP-seq) regulated by EZH2 (*siEZH2* RNA-seq) with low FLASH signal (no binding at the RNA level). In *group 2*, there are the targets with high PRC2-RNA signals (FLASH) over the genes bound to the nascent transcript, but with low occupancy of EZH2 (ChIP) and pronounced MEG3 enrichment on the chromatin. We focused on targets in group 1, regulated by EZH2 at the DNA level in a MEG3-dependent manner. A subset of genes had functions in cell adhesion molecule binding and again belonged to the *integrin cell surface interactions pathway*. These integrin targets do not interact at the RNA level with EZH2 but are specifically regulated by it (Figures 4B and S9). Among the top 50 *siEZH2* genes, *ITGA4* is a direct target, together with *ITGB1*. In Figure S6B, ii, *ITGA4* was also upregulated due to *MEG3* KD. Therefore, *ITGA4* is an apparent mutual target of MEG3/EZH2 (Table S8). The integrin *ITGA4* exists as a dimer with ITGB1 subunit in the cell known as α4β1 (CD49d/CD29), which is a cell adhesion receptor known to bind fibronectin (FN1, selective for the CS1 domain) and VCAM1 (vascular cell adhesion molecule 1) as a counter receptor that is crucial for controlling the focal adhesion formation and cell migration.

MEG3 occupancy by ChIRP was seen within the *ITGA4* promoter in HUVECs (Figure 4C). Both H3K27me3 peaks of available GEO datasets from HUVECs and in-house EZH2 peaks were also detected in the *ITGA4* promoter region and aligned with the MEG3-ChIRP peaks. Depletion of MEG3 (*MEG3* KD) resulted in a visible loss of EZH2 signal from this promoter area. Subsequent ChIRP-qPCR showed an enrichment of MEG3 binding compared with LacZ control at three sites (probe areas 1, 2, and 3) within the *ITGA4* promoter (Figure 4D), and this binding corresponds to EZH2 ChIP-seq signal in the area (Figure S8A). There is a CpG island of 1,268 bp covering the *ITGA4* region of probe area 2 where the signals converge, chr2:181,457,035–181,458,302 (green) with all other PRC2 components also visibly binding (Figure S8A).

MEG3 depletion results in increased expression of *ITGA4* in HUVECs (Figures 4E and S5C). The public dataset of murine Meg3-depleted C2C12 myoblasts further corroborates that *ITGA4* is a direct target of MEG3 (Figures S6D and S6E).[30,31] We next performed ChIP-qPCR to quantify the levels of EZH2 and H3K27me3 repressive marks in HUVECs and observed their enrichment at the

Table 2. Functional profiling of differentially expressed genes in EZH2 ChIP-seq from control and MEG3-depleted ECs

ID	Source	Term ID	Term name	p_{adj} (query_1)
1	GO:MF	GO:0050839	cell adhesion molecular binding	8.991×10^{-5}
2	GO:MF	GO:1904929	coreceptor activity involved in Wnt signaling pathway, planar cell polarity pathway	1.619×10^{-3}
3	GO:MF	GO:0015085	calcium ion transmembrane transporter activity	2.137×10^{-2}
4	GO:BP	GO:0007155	cell adhesion	9.053×10^{-5}
5	GO:BP	GO:0022610	biological adhesion	1.083×10^{-4}
6	GO:BP	GO:0098609	cell-cell adhesion	2.892×10^{-3}
7	GO:BP	GO:0098742	cell-cell adhesion via plasma membrane adhesion molecules	4.212×10^{-3}
8	GO:BP	GO:0034330	cell junction organization	9.316×10^{-3}

Molecular function (MF) and biological pathways (BP) of all unique RefSeq genes within TSS ± 3 kb, sorted by occupancy in control vs. MEG3-LNA GapmeR (10 nM, *MEG3* KD) HUVECs. Reduction or depletion in EZH2 signal is seen in 10% of genes mostly belonging to biological adhesion, cell-cell adhesion, and cell junction. The total list of regulated genes is given as Table S8 csv file.

promoter region of *ITGA4*. Assessment of the enrichment on the *ITGA4* promoter following MEG3 depletion showed a reduction in both EZH2 and H3K27me3 signals at the *ITGA4* promoter region (Figure 4F). We conclude that the PRC2 complex binds and is enzymatically active at the *ITGA4* site. Our findings prove that the loss of MEG3 compromises the H3K27me3 landscape, as it reduces PRC2 binding to *ITGA4*. Accordingly, PRC2 requires binding of MEG3 for chromatin localization and methyltransferase activity in the promoter region of *ITGA4*.

MEG3-EZH2-dependent regulation of *ITGA4* is required for EC function

To gain further insight into the functional significance of the interaction of EZH2 with MEG3, we determined how pharmacological inhibition of EZH2 enzymatic activity affected cell function and gene expression. We used a selective chemical probe known to prevent allosteric activation of the catalytic activity of PRC2 (A-395[32,33]). A-395 is a potent antagonist of the H3K27me3 binding functions of EED protein, and it disrupts the trimeric PRC2 complex and blocks EZH2 activity in ECs. Next, we performed ChIP-qPCR against EZH2 and H3K27me3. A-395 reduced the ChIP signals of EZH2 and induced endothelial chromatin remodeling by depleting H3K27me3 from the *ITGA4* promoter; amplified by two sets of primers against this promoter region (Figure 5A). Treatment with A-395 led to increased expression of *ITGA4* compared with control cells (Figure 5B). Similarly, an increase in *ITGA4* transcript level was observed following MEG3 depletion in ECs (Figure 5C). We used immunocytochemistry and western blot analysis in Figure 5C, i and ii, and identified an increase in ITGA4 protein (human protein atlas: https://www.proteinatlas.org/ENSG00000115232-ITGA4) levels following MEG3 depletion or PRC2 inhibition; (Figure 5C, ii, quantification of the blot in Figures S8B and S9). This further confirmed that both MEG3 and PRC2 regulate ITGA4 protein expression.

We also assessed the subcellular distribution of MEG3 that is chromatin associated and predominantly localized in the nucleus. MEG3 co-localizes with EZH2 on the chromatin in ECs (Figures S7A–S7C). Surprisingly, we observed a shift in the cellular distribution of MEG3 when ECs were treated with the A-395 inhibitor, with increased cytoplasmic occupancy of MEG3 (Figure 5D) and we reasoned that MEG3 could be removed from the chromatin. We therefore performed ChIRP in ECs treated with the A-395 inhibitor of PRC2 and found less MEG3 enrichment at the *ITGA4* promoter region on the chromatin compared with non-biotinylated control probes or the DMSO control (Figure 5E).

Finally, we assessed EC functionality following treatment with A-395. By measuring the cell migratory capacity and determining the speed of migration, we observed that A-395 rendered ECs with a greater migratory capacity and increased the closure of scratch assay *in vitro* compared with control (DMSO) (Figure 5F). The interaction of cells with fibronectin (FN) is specific and mediated by integrin receptors at the cell surface.[34] The engagement of integrins by FN triggers a signaling cascade inside the cells that ultimately culminates in cell adherence and spreading. The cell index was determined as a measure of cell attachment to FN that leads to increase of resistance and adhesion within 3 h. Cells were successfully depleted of *ITGA4* (Figure S5D). A-395 treatment efficiently increased the cell migration and attachment compared with control (Figures 5F and 5G). Reduced migration and adhesion capacity were observed in *ITGA4*-depleted cells, but A-395 treatment reverted this pattern.

Inhibition of EZH2 *in vivo* promotes arteriogenesis

Endothelial integrins are involved in vascular lumen formation of arteries, angiogenesis, inflammatory processes, and vessel wall remodeling.[35] We investigated the regulation of the MEG3-EZH2-ITGA4 axis using a model of post-ischemic vascularization (i.e., the model of hindlimb ischemia induced by femoral ligation). Mice were treated with A-395 (i.p. 10 mg/kg twice/week; or vehicle control) to inhibit EED/EZH2 enzymatic activity demonstrated by the decreased of the level of H3K27me3 in the adductor muscles and ECs (Figure 6A). A-395 treatment increased the formation of collaterals (shown is an increased number of arterioles without producing an increase of capillaries) in mice following ischemia compared with the control (Figure 6B). A-395 treatment has not increased the blood flow following hindlimb ischaemia (Figure 6C), only an increase is observed in the overal mean ratio of recovery compared to day 0 (Figure S8C). Respectively total percentage (%) of vessels positive for ITGA4, and % of arterioles positive for ITGA4 was increased with A-395 compared with control (Figure 6D *i*, *ii*). In summary, the dissociation of the MEG3-EZH2 complex using A-395 chemical probe to disrupt PRC2 complex in mice has improved arteriogenesis by increasing the expression of endothelial *ITGA4*.

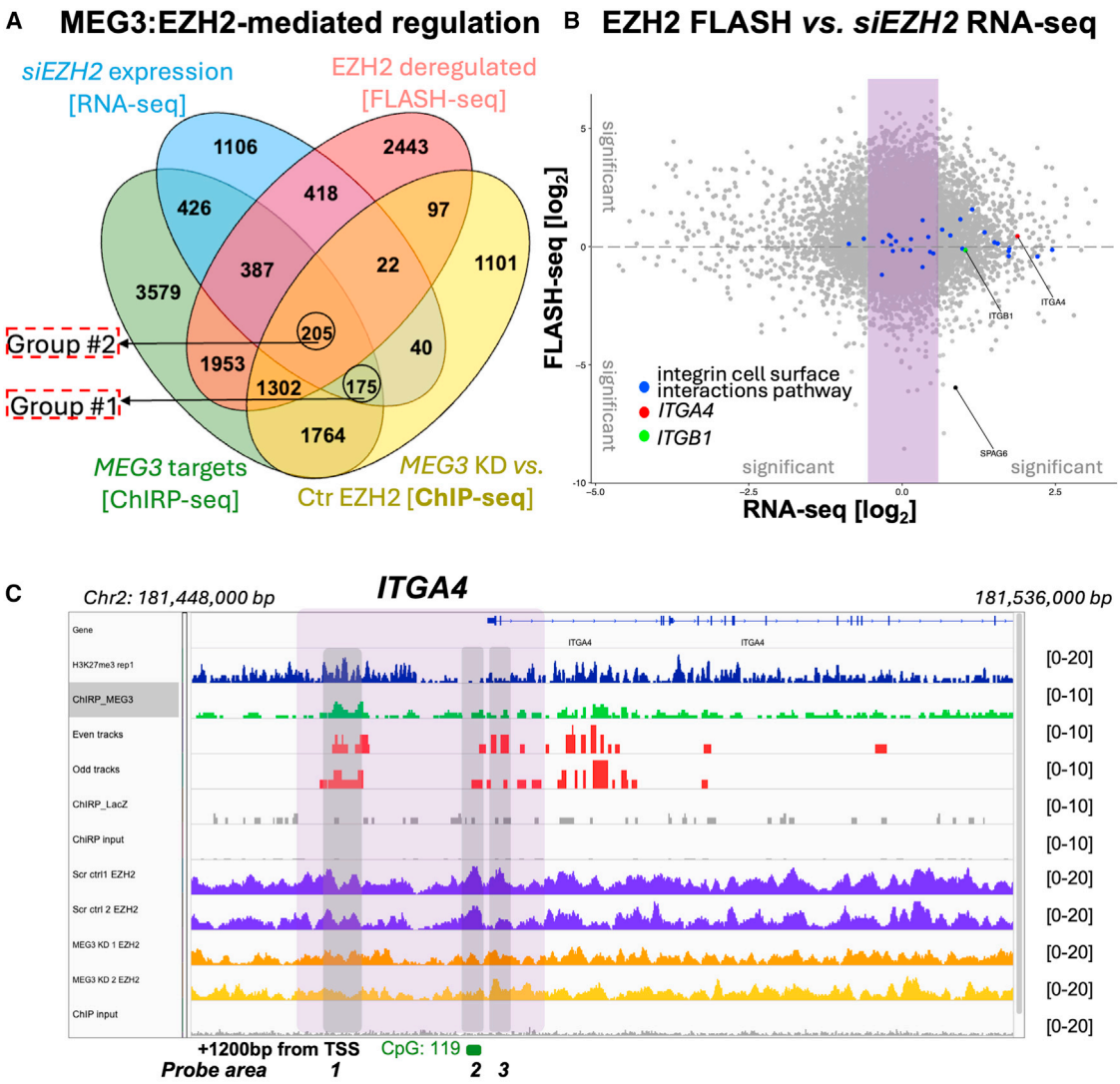

(legend on next page)

DISCUSSION

The results of this study represent several novel findings: first, that EC lncRNA-MEG3 is bound by EZH2 via stable secondary structure elements. Second, we demonstrate a MEG3-dependent mechanism of EZH2 engagement with integrin α, *ITGA4*, to epigenetically repress its expression in ECs. Following comprehensive exploration, we demonstrated the significance of the *ITGA4* signaling pathway *in vivo* for the collateral formation in hindlimb ischemia. More, we also show that PRC2 inhibition could counteract ischemia-induced endothelial dysfunction and vascular remodeling by dissociating the EZH2-MEG3-ITGA4 axis.

Many endothelial lncRNAs mediate gene expression and could guide context-specific regulation of PRC2 activity. Other immunoprecipitation approaches to gain insight into EZH2 binding RNA in ECs gave inconsistent data, but the use of FLASH now provided us with biochemical evidence for direct physical and functional interactions. EZH2 binding is constrained to MEG3 hybrid interactions, indicating conserved pseudoknot structures.[36] This is also consistent with *in silico* predictions that MEG3 is highly structured, due to its high content of G-C base pairs (57%).[13,36] The identification of secondary structures within the MEG3 molecule as docking sites for EZH2 binding indicates that the MEG3 structure is a direct intermediate for PRC2 recruitment onto chromatin. The G-rich motif sequences are recognized by EZH2 and could aid structures such as RNA G-quadruplex formation (rG4), but we did not study this.[37] There is now a need to ascertain whether other MEG3 splice variants with different MEG3 exonic organization have similar functions and exhibit different levels of interactions or MEG3 structures.

While EZH2 is more preferentially associated with the MEG3 exon, the endothelial MEG3-binding loci from ChIRP were mostly recovered in intergenic and intronic regions. Crossing the MEG3 genomic loci with EZH2 genomic occupancy showed clear overlap in a subset of exons and promoters. Among common target genes, the enrichment for functions in angiogenesis, preferentially integrin-related functions in adhesion and extracellular matrix formation were seen. Integrins, the heterodimeric cell adhesion molecules, recognize a variety of proteins on the surface of other cells or in the ECM. Therefore, they are essential for all processes critical to inflammation and angiogenesis such as cell adhesion, sprouting, and migration following injury.[35] Our data show the expression of *ITGA4* in ECs is essential for migratory processes and for regulation of FN-stimulated cell adhesion or adhesion-dependent signal transduction. It was therefore unsurprising that MEG3 occupies these regions and integrin (*ITGA4*) was transcriptionally upregulated upon MEG3 depletion. Integrin-mediated EC adhesion to ECM triggers remodeling of the cytoskeleton of ECs that precedes vessel sprouting, also exactly the processes that are inhibited by MEG3.[29,38] *ITGA4* codes for α4, the subunit of the α4β1 integrin receptor dimer that in ECs ensures high affinity for FN and hence controls processes of focal adhesion and cell migration.[39] Moreover, α4β1 is an important receptor for EC homeostasis, which mediates proliferative responses,[40,41] whereas β1 integrin is required for collateral formation, and widening of the arterial lumen following hindlimb ischemia.[42] Here, we identified a previously unknown mechanism by which *MEG3* regulates *ITGA4* in an endothelium-dependent manner, unlike its role in the TGF-β pathway.[43] In our ChIRP dataset we did not observe strong MEG3 targeting of TGF-β in the endothelium, despite established similarities with the Mondal et al.[43] dataset (overlap of 2,933 hits upon correlation). Hence, our findings signify a context-specific role of endothelial MEG3, as seen in myoblast identity,[30] to regulate the α4 integrin expression and integrin signaling and promote EC function following ischemia.

Our extensive bioinformatic approaches have exposed a mutual role for MEG3 and EZH2 in regulation of *ITGA4* that mediated the endothelial function *in vitro* and in our murine model. Removal of MEG3 abolished the loss of migratory capacity and increased the sprouting capacity of ECs; two key processes during the initial stages of

Figure 4. MEG3:EZH2-regulated targets in ECs

(A) Using a Venn diagram, logical relationships are displayed between genes by plotting the EZH2-FLASH RNA gene interactome (pink) against RNA-seq data for genes that are differentially expressed following EZH2 knockdown in HUVECs (blue) (these are *de novo* analyzed GEO RNA-seq data (GSE71164) of Scr vs. EZH2). Next, MEG3 ChIRP-seq peaks (green) are displayed against EZH2 ChIP-seq intensities over loci (yellow) obtained following *MEG3* KD in HUVECs. We focused on targets in Group 1, that are regulated by EZH2 at the DNA level, in a MEG3-dependent manner. (B) Correlation between gene expression levels and FLASH signal. Gray, expressed RefSeq genes with reproducible FLASH signal consistently detected in RNA-seq. Blue, genes with the highest RNA-seq signals and no reproducible FLASH signal belonging to integrin cell surface interaction pathway. Red, expressed *ITGA4* gene; green, *ITGB1* gene, without reproducible FLASH signals. Data are from two biological replicates of each EZH2 FLASH sample and three biological replicates of EZH2 RNA-seq samples (Scr vs. siEZH2, GSE71164). (C) Genomic tracks showing ChIRP-seq signal (MEG3 and LacZ) in HUVECs over the *ITGA4* gene region. The updated tracks for ChIRP-seq show called peaks using MACS2. The two ChiRP tracks are from biological replicates of even and odd probes, which have been combined in all MEG3 tracks from two experiments. The MEG3 binding site is located upstream of the *ITGA4* gene in the promoter region, and it overlaps with the H3K27me3 signal and EZH2 signals, and it overlaps with the EZH2 signal in the promoter region of the gene. The EZH2 ChIP-seq tracks over *ITGA4* regions are also presented in duplicates for Scr control and MEG3-depleted HUVECs (MEG3 KD, 10 nM). Within the *ITGA4* promoter region where the named signals converge there is a CpG island of 1,268 bp covering chr2:181,457,035–181,458,302 (green). This same pattern of EZH2 and other PRC2 components occupancy is observed on UCSC representation of *ITGA4* regulatory region (see Figure S8A). (D) MEG3-ChIRP validation by qPCR, n=3 independent experiment in duplicates. Analysis of MEG3 binding was done using primers against *ITGA4* probe areas 1, 2, and 3 as marked in corresponding signal under (C). qPCR was performed in triplicate. The signal was related to LacZ control ChIRP to calculate the enrichment and background level was <1. (E) *ITGA4* expression in HUVECs depleted of MEG3 (10 nM, 48 h) vs. LNA GapmerR control from n=6 independent experiments compared using a t test. (F) ChIP-qPCR enrichment for EZH2 and H3K27me3 over the *ITGA4* promoter region using primer set *ITGA4*-2 in HUVECs depleted of MEG3 (10 nM) vs. LNA GapmeR control (control). qPCR was performed in triplicates from n=4 independent experiments. The signal is expressed as percent IgG control. Both EZH2 and H3K27me3 signals are reduced in *MEG3* KD samples. A representative graph is from n=3 independent qPCR experiments with data showing mean ± SEM.

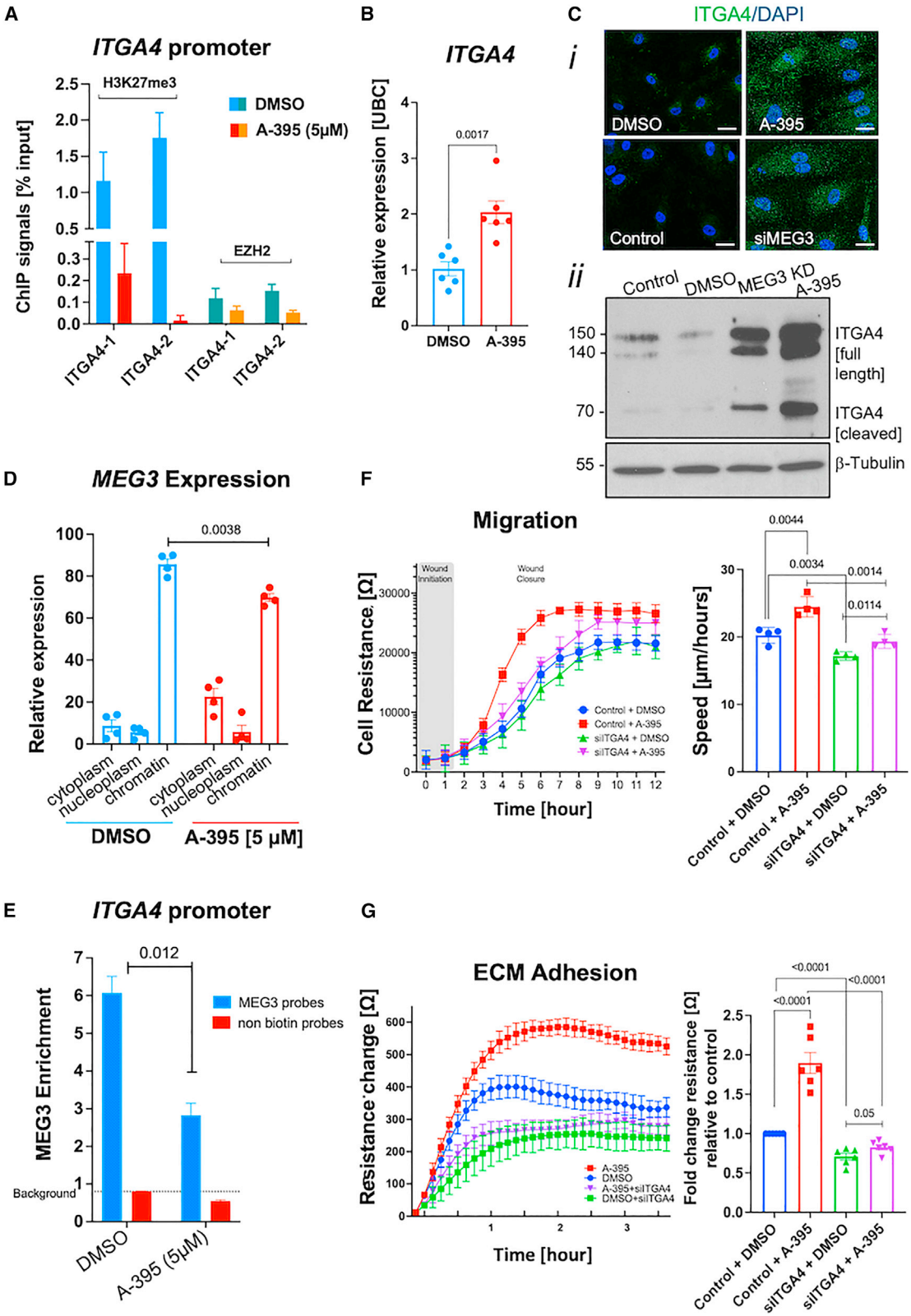

(legend on next page)

vascularization. The presence of H3K27me3 on *ITGA4* precedes the recruitment of PRC2 that promotes propagation of H3K27me3 mark. Since the MEG3:EZH2 interaction was unraveled at the genomic region of *ITGA4* where the PRC2 is enzymatically active, we reasoned that H3K27me3 permits the assembly of all other PRC2 components, (EED and SUZ12) to maintain its canonical function at this chromatin loci. Occupancy of the *ITGA4* region by EZH2 results in binding to MEG3, which further stimulates EZH2 enzymatic activity. MEG3 could act as a triplex forming lncRNA here and use a functionally important mechanism to alter chromatin architecture and regulate *ITGA4* expression.[44,45] This is in line with PRC2 using RNA binding to enhance the long-range chromosome folding and H3K27me3 spreading.[46] Accordingly, in the absence of MEG3, the genomic occupancy and spread of EZH2 over *ITGA4* were reduced, along with H3K27me3 over the *ITGA4* promoter. Given the importance of MEG3-mediated chromatin remodeling for post-ischemic re-vascularization, these findings have important implications for vascular diseases associated with cardiac and peripheral ischemia.[35]

Use of PRC2 inhibitors, or repurposing some of them to stimulate specifically post-ischemic angiogenesis, could offer useful means for regulation of adhesion signaling pathways and integrin production by ECs. Integrin activation in arterioles is required for collateral growth following ischemia (arteriogenesis) in the mouse hindlimb ischemia model[42] and is associated with improved recovery following myocardial infarction.[47] When we employed a small chemical probe A-395, and administered it to block the activity of EED/EZH2 during ischemia, it unlocked *ITGA4* expression and led to an increase in arteriole numbers in the adductor muscles. A-395 improves EC migration and appears to have a prominent effect on vessel maturation, unlike vessel sprouting. This mechanism was specific for arteriogenesis only, as there were no observed changes in the number of capillaries in the same experimental conditions. The effect of A-395 could also be coming from other cell types involved in vessel maturation. Moreover, an increased expression of integrins contributes toward the vessel maturation,[42] and the formation of collaterals requires β1 integrin for endothelium-dependent vasodilation in hindlimb ischemia. Treatment of mice by intraperitoneal injection of EZH2 also involved repeated injections prior to limb ischemia, which may result in off-target effects, and hence does not selectively interfere with EZH2 inhibition in the muscle. However, the data reported here are consistent with the role of MEG3 or EZH2 in driving limb ischemia and show significant arteriogenesis following treatment with A-395. As a therapeutic benefit, pharmacological inhibition of the EED-EZH2 interaction[32] could be a novel strategy to activate *ITGA4* signaling during myocardial infarction to increase the resilience of ECs for prevention of cardiac remodeling.

In conclusion, we demonstrate that EZH2 directly targets structured MEG3 in ECs, which is in turn involved in guiding EZH2 to transcriptionally repress integrin signaling. Thereby, dissociation of MEG3-EZH2 promotes arteriogenesis by stimulating *ITGA4* expression and protein levels. We have shown proof of concept that specific EED protein-protein interaction inhibitor (A-395), which inactivates PRC2, can also alter RNA binding properties of EZH2/PRC2 and dissociate MEG3 chromatin interactions, promoting post-ischemic re-vascularization.

MATERIALS AND METHODS

Animal work

All scientific procedures involving mice were covered by the project and personal licenses issued by the UK Home Office, and with approval from the University of Bristol and the University of Edinburgh. Experiments were performed in accordance with the Guide for the Care and Use of Laboratory Animals (Institute of Laboratory Animal Resources, 1996) and in accordance with Animal Research Report of *in vivo* Experiments (ARRIVE) guidelines.

In vivo *model of therapeutic angiogenesis with Doppler analysis*

To determine the potential of A-395 selective chemical probe for vascular regeneration *in vivo*, a mouse model of therapeutic angiogenesis, with a hindlimb ischemia was used. Surgery was performed to

Figure 5. Inhibition of EZH2 de-represses ITGA4 and improves EC function

(A) ChIP signal enrichment vs. 1% input for EZH2 and H3K27me3 mark over the *ITGA4* promoter (regions 1 and 2) in HUVECs treated with A-395 (5 μM, 24 h) vs. control (DMSO). The expression was measured using two sets of primers against the same promoter region of *ITGA4*. Representative graphs are average of 3 independent qPCR experiments and data are mean ± SEM. (B) *ITGA4* expression in the presence of A-395 vs. DMSO control, n=6 independent experiments compared using a t test. (C) (i) Immunostaining for ITGA4 protein levels in ECs treated with A-395 (5 μM) vs. DMSO, or upon MEG3 depletion (MEG3 KD, using LNA GapmeRs, 10 nM 48 h). Scale bars, 400 μm (magnification ×200). (ii) Western blot staining for ITGA4 protein as in (i). Staining was related to β-tubulin control and quantification with densitometry measurement and a full blot in Figures S8A and S9. (D) Intracellular localization of MEG3 (chromatin-associated lncRNA) between different cellular compartments in HUVECs treated with A-395 vs. DMSO. Using A-395 (5 μM, 24 h) chemical probe, the distribution of MEG3 has shifted from the nucleus (where it was highly chromatin bound) into the cytoplasm. Representative bars were compared by t test and one-way ANOVA. (E) MEG3-ChIRP followed by qPCR, n=3, analysis of MEG3 binding over the *ITGA4* promoter region in HUVECs treated with A-395 (5 μM, 24 h) vs. DMSO. MEG3-ChIRP lysates from HUVECs treated with A-395 resulted in reduced engagement of MEG3 with the *ITGA4* site compared with either DMSO control or ChIRP with non-biotinylated probes. The non-biotin probes served as a negative control, and we detected the background level <1. (F) Measure of cell migratory capacity using ECIS functional analysis in ECs depleted of *ITGA4* (50 nM) and treated with control or A-395 (5 μM, 24 h). The data showing ECIS trace (left-hand side) are mean ± SD as calculated by the ECIS machine. The graph on the right is mean ± SEM with n=4 replicates, and each value obtained as mean of three technical replicates. p values were further obtained by Student's t test comparisons of individual groups, as shown.

(G) Adhesion assay was assessed using ECIS functional analysis. Fibronectin, FN (20 μg/mL) was used to coat the culture plates and assess adhesion of ECs following cell pre-treatment with A-395 (5 μM, 24 h). The cell index was determined as a measure of cell attachment to FN that leads to increase of resistance and adhesion. The difference in resistance change was calculated over 3 h. Experiments were performed in triplicate (technical replicates). The data showing ECIS trace (left-hand side) are mean ± SD as calculated by the ECIS machine, and the graph on the right is mean ± SEM with n=6 replicates.

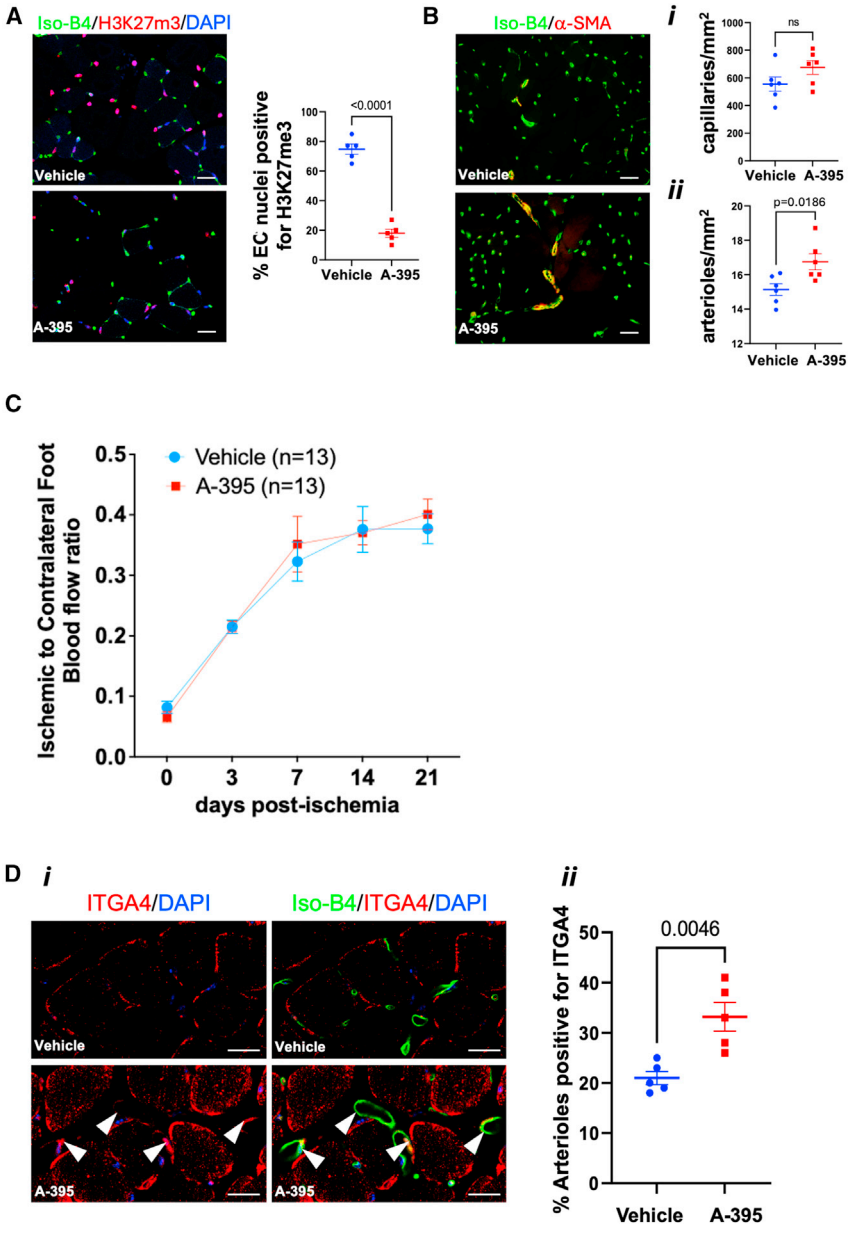

Figure 6. Hindlimb ischemia was performed in mice (n=13) that were injected with vehicle (water) or A-395 (i.p. 10 mg/kg twice/week) to inhibit EZH2 enzymatic activity for 3 weeks.

Muscle tissue was collected at day 21 and processed for histology. (A) Staining was done for H3K27me3 and isolectin B4 (Iso-B4), displaying nuclear positivity with strong intensity in vehicle control. A-395 treatment decreased total H3K27me3 staining, as compared by t test ($p < 0.0001$), while seemingly increasing isolectin B4. Scale bars, 400 μm (magnification ×200). (B) Staining for capillaries (Iso-B4) and arterioles (α-SMA) was also performed to assess arteriogenesis in mice. The data show increased area of staining for Iso-B4 dye and α-SMA in A-395 *vs*. vehicle control treated mice with limb ischemia, $p < 0.05$. Scale bars, 400 μm (magnification ×200). (C) The ratios of ischemic to contralateral foot blood flow represented at 0, 3, 7, 14 and 21 days post hindlimb ischemia in mice (n=13) remained unchanged between A-395 treatment and control; data is mean ± SEM, compared using 2-way ANOVA. (D) *i* In the muscle sections A-395 has increased the total percentage (%) of vessels positive for ITGA4 (red, left) within/in the vicinity of the Iso-B4-positive cells (green, right), when compared with the vehicle control Scale bars, 100 μm (magnification ×400); *ii* Percentage (%) arterioles stained with α-SMA and positive for ITGA4, has increased in sections of A-395 treated mice comapred with control. Representative points were compared using *t*-test, $p < 0.01$.

induce left femoral artery ligation in 12-week-old male C57BL/6J mice. A-395 (10 mg/kg dose i.p. at day 0 and every 3 days for 21 days) or vehicle (H_2O) was administered *in vivo*. On the day of surgery mice were anesthetized using 3% isoflurane in air, and the fur above the left femoral triangle shaved. Mice were maintained on 2%–3% isoflurane in air. After checking for depth of anesthesia using the pedal reflex, the skin above the femoral artery was sterilized (chlorhexidine in alcohol) and the remainder of the mouse covered using transparent sterile drapes. Aseptic technique was used throughout the surgical procedure to induce left femoral artery ligation. The basal foot blood flow was assessed in two groups of male mice (n=13) by color laser Doppler (Moor, UK) to ensure complete ischemia within 30 min following surgery (day 0, D0), and thereafter at 3, 7, 14, and 21 days to monitor the recovery, with thermal scans generated for each animal at given timepoint. The blood flow measurements were conducted exactly as described before.[8] After administration of long-acting analgesic buprenorphine (Vetergesic, 0.01 mg/kg dose s.c.), the animals were allowed to recover under observation. The animals were closely observed daily for the first 7–10 days post-surgery and a well-being and behavioral clinical assessment performed. No animals required additional analgesia. At this point, when animals have recovered, A-395 or vehicle were administered to each group of mice (n=13). After 21 days, final blood flow measurement was conducted; the ratio of left to right foot blood flow was calculated for further statistical data analysis. Anesthetized mice were killed by exsanguination for organ removal. Adductor muscles were collected and processed for histology. Paraffin cross-sections were blocked with normal goat serum, incubated with anti-H3K27me3 (CST) and anti-ITGA4 (1:200, PeproTech) primary antibody or biotinylated isolectin-B4 (Thermo Fisher Scientific) overnight at 4°C, and then incubated with Alexa Fluor 555-conjugated anti-rat IgG antibody or streptavidin Alexa Fluor 488-conjugated (1:1,000) (Thermo Fisher Scientific). High-power fields were captured

(at 400×) and the number of vessels per field were counted. At least 30 randomly chosen fields were evaluated per sample, in a blinded experiment. Isolectin B4 (Iso-B4)-positive vessel area was quantified using ImageJ software and expressed per square micrometer. Staining for arterioles (α-smooth muscle actin, α-SMA) was performed to assess vessel growth as angiogenesis.

EC culture and treatment and transfection

HUVECs (C-12203) and human dermal microvascular endothelial cells (C-12212) were purchased from Promocell, Germany, and cultured in the recommended growth medium (EGM2-MV2 or MV, respectively) according to the manufacturer's instructions under 5% CO_2 at 37°C. Hypoxia was stimulated in a Coy chamber with a gas mixture of 1% O_2, 5% CO_2, and 94% N_2 (Coy Laboratory Products). Cell preparation for experiments varied in the size and number of plates used and the quantity of cells harvested. Cryopreserved cells were brought into culture and incubated in complete medium to adhere to flasks. Fresh medium was added to remove residual DMSO after 24 h, and cells were incubated in their first passage for 48 h. Medium was replaced every 48 h and cells were passaged once reaching 80%–90% confluency and expanded to passage P3 then frozen for further use. Cells were cultured between passage P4 and P8 for 16 duplication times (P8). All cells described in the following experiments were used at P5 or P6. Cells were washed with PBS, detached using trypsin/EDTA (1×, Life Technologies) and plated onto plates of desired size. Cells were plated on 6-well plates at 80% confluence and left to attach overnight before pre-treating them with A-395 (Sigma, SML1923) for 24 h using 5 μM final concentration with 0.01% DMSO in water. For transfection experiments, cells were seeded onto a 12-well plate, for 24 h. Next day OPTIMEM medium was added for 1 h before addition of transfection complexes prepared by mixing lipofectamine iMax (Thermo Fisher Scientific) with LNA GapmeRs against MEG3 (10 nM, QIAGEN). Cells were incubated (6 h), then complexes and optimum replaced with medium for further 48 h.

RNA extraction and quantitative real-time analysis

Total RNA was extracted using miRNeasy kit (QIAGEN) or Monarch kit (New England Biolabs [NEB], no. T2010). RNA concentration and purity were assessed using a NanoDrop2000 Spectrophotometer (Thermo Fisher Scientific). For mRNA analysis, RNA was reverse transcribed using a LunaScript reverse transcription Kit (NEB, no. E3010). cDNA amplification was performed on a QuantStudio 5 Flex (Thermo Fisher Scientific) Real-Time System in a 384-well plate. A Luna qPCR SYBR Master Mix (NEB, M3003) was used along with specific primers to determine the expression of MEG3 and housekeeping genes using an Applied Biosystems QuantStudio 5 Real-Time PCR Detection System. The comparative delta cycle threshold (Ct) value method was used for qPCR analysis. Ct values represent the number of PCR stage cycles required for cDNA of a gene of interest to be amplified enough for the fluorescent signal from the reaction to exceed a defined threshold. A full list of primers and reagents is given in Table S10.

Subcellular fractionation (to obtain nuclear, chromatin, and cytoplasmic RNA) with qPCR

For subcellular isolation of RNA, HUVECs were plated onto 10-cm^2 dishes at P5. Medium was changed and cell plates were treated with A-395 or DMSO for 24 h. Cells were collected and gently lysed in hypotonic lysis buffer to obtain supernatant (cytoplasm) and pellet (nuclei) using low-speed centrifugation that was sufficient to pellet and wash nuclei from HUVECs. Further fractionation steps were performed to separate the nuclear fraction into chromatin and nucleoplasm following sonication. The full protocol was described previously.[48,49]

Cytoplasmic hypotonic lysis buffer contained 10 mM Tris (pH 7.5), 10 mM NaCl, 3 mM $MgCl_2$, 0.3% (v/v) NP-40, 10% (v/v) glycerol. Buffers were prepared using nuclease-free water with addition of protease inhibitor mix, prepared freshly before use and stores on ice). Nuclei wash buffer: 0.1% (v/v) Triton X-100, 1 mM EDTA, 25 μM α-amanitin, 40 U SUPERase.IN, 1× protease inhibitor mix, in 1× PBS. Nuclei lysis buffer: 20 mM Tris (pH 7.5), 150 mM KCl, 3 mM $MgCl_2$, 0.3% (v/v) NP-40, 10% (v/v) glycerol, 10 U SUPERase.IN, 1× protease inhibitor mix. MSW lysis buffer: 10 mM Tris-HCl (pH 7.0), 4 mM EDTA, 0.3 M NaCl, 1 M urea, 1% (v/v) NP-40. The buffers were prepared using nuclease-free water and stored at 4°C for up to 6 months.

Pelleted nuclei were washed, lysed, and split to directly isolate the total nuclear RNA. Remaining nuclei were diluted in MWS for 30 s and incubated on ice for 10 min before centrifugation at 1,000 × *g* at 4°C for 3 min. The supernatant (nucleoplasm fraction) and pellet (chromatin) were collected into TriaZol to isolate RNA.

The RNA extraction was performed following a Monarch kit (NEB, no. T2010). RNA was precipitated with 60 μL of 3 M sodium acetate (pH 5.5), 2 μL of GlycoBlue (15 mg/mL), and 500 μL of RNase/DNase-free H_2O, and extracted from each fraction, from three independent experiments as described above. Following RNA quantification using NanoDrop, reverse-transcription (RT)-qPCR reaction was carried out in duplicate, with total of 300 ng of purified RNA being converted to cDNA using 1× LunaScript RT SuperMix in 20 μL reactions and standard reaction conditions (25°C/2 min, 55°C/10 min, 95°C/1 min). qPCR detection was performed using the Luna Universal qPCR Master Mix (NEB, M3003) and included 1 μL of neat cDNA product as a template, with triplicate reactions for each target against MEG3, UBC, or NEAT1. Results were evaluated for efficiency and lack of non-template control amplification.

To study the cellular localization of MEG3, the qPCR levels of MEG3, *U1* snRNA, NEAT1, and UBC in the chromatin, nucleus, and cytoplasm were plotted as percentage, defined as: percentage chromatin = (MEG3 quantified in RNA chromatin fractions)/(U1 snRNA quantified in total fraction RNA); nucleus = (MEG3 quantified in RNA nuclear fractions)/(NEAT1 quantified in total fraction RNA); and percentage cytoplasm = (MEG3 quantified in RNA cytoplasmic fractions)/(UBC quantified in total fraction RNA); using *U1* snRNA,

NEAT1, UBC, or 18S as loading controls of chromatin, nucleus, cytoplasm, and total cellular fractions, respectively.

UV crosslinking of cells

For plates to be treated with UV, 15-cm culture dishes with confluent HUVECs were washed in ice-cold PBS. PBS was removed before placing cells on a bed of ice and crosslinking with 400 mJoules/cm^2 UVB frequency λ = 254 for 2 min in a CL-1000 UltraViolet Crosslinker UVP Stratalinker (Stratagene). Cells were washed twice in ice-cold PBS (300 rcf, 5 min, 20°C) and scraped to collect the pellet (16,000 rcf, 5 min, 4°C). During the final wash, cells were resuspended in 1 mL PBS and transferred into a 1.5-mL Eppendorf then centrifuged again and the pellet was immediately used in a fractionation step or cell lysis.

FLASH

The approach used is similar to that reported for CLASH,[50] whereas RNA-protein interactions were captured in growing cells using UV crosslinking (as above) and antibodies for affinity purification of endogenous RNA-protein complexes instead of FLAG-tagged protein.[21] In brief, formaldehyde crosslinking is used during the purification step to stabilize binding of the covalent bait protein-RNA complex to the protein A beads. This step allows column washes under highly denaturing conditions, hence assuring reliable downstream hits.

HUVECs were cultured as described, grown to 80% confluency, UV crosslinked, and cell pellet collected, as above. The pellet was lysed in ice-cold TM150 buffer (20 mM Tris-HCl [pH 7.4], 150 mM NaCl, 0.4% NP-40, 2 mM $MgCl_2$, 1 mM DTT, protease inhibitors [Roche, complete, EDTA-free], RNAse inhibitor [Promega]). Ten microliters of RQ1DNAse (Promega) was added and the samples were mixed by pipetting and incubated for 10 min at room temperature to break genomic DNA. Lysates were centrifuged in an Eppendorf mini centrifuge (14,000 rpm, 4°C, 10 min) and supernatant was collected.

Affinity purification

To precipitate EZH2, we used 20 μL of anti-EZH2 rabbit monoclonal antibody (D2C9 clone, CST, no. 5246S) and crosslinked cell lysates of HUVECs. We used non-immune (mouse or rabbit) IgG and ribonucleoprotein (RNP) rabbit polyclonal anti-hnRNPAB (PA5-27549, Thermo Fisher Scientific) as a control (see Table S10). Immunoprecipitation was done for 2 h at 4°C, then 50 μL Protein A beads (LSKMAGA02, Millipore) were added for another 60 min. The RNP complexes bound to the beads were washed twice with PBS-WB buffer (PBS, +150 mM NaCl, 2 mM $MgCl_2$, 0.4% NP-40), and treated with 0.5 U RNaseA + T1 mix (RNace-IT, Stratagene) for 10 min at 20°C, then washed again twice with PBS-WB buffer and once in PBS. These complexes were crosslinked on beads in 0.1% formaldehyde (PFA) (Life Technologies no. 28908) in PBS for 2 min, then PFA was quenched by addition of glycine to 0.2 M and Tris-HCl (pH 8) to 0.1 M. Crosslinked complexes were subjected to 3× denaturing washes in UB (50 mM Tris [pH 7.4], 2 M urea, 0.3 M NaCl, 0.4% NP-40) and 4× washes with PNK buffer (50 mM Tris-HCl [pH 7.5], 10 mM $MgCl_2$, 50 mM NaCl, 0.5% NP-40, 1 mM DTT) to remove non-specific interactions. Subsequent steps were identical for FLASH as described for CLASH.[50]

RNA end modification and linker ligation

The complexes were treated with TSAP phosphatase (Promega) for 40 min at room temperature. Between all enzymatic reactions, immobilized complexes were washed once with UB and three times with PNK buffer. Phosphorylation of RNA was carried out with 40 units T4 PNK (NEB), first with P32-labeled ATP for 45 min, then a further 20 min with 1 mM cold ATP at room temperature. The reactions should provide 5′ phosphates needed for downstream ligations.

Protein-bound RNA molecules were ligated together and with 3′ linker (1 μM miRCat-33, IDT) overnight using 40 units of T4 RNA ligase 1 (NEB) at 16°C. This reaction created RNA hybrids and single RNA molecules ligated to miRCat linker.

Then barcoded 5′ linkers (final concentration 5 μM; IDT, one for each sample) were ligated with RNA ligase 1 in its buffer with 1 mM ATP for 3–6 h at 20°C (see Table S10). The complexes were eluted off the beads by boiling for 3 min in NuPAGE protein sample buffer with 100 mM Tris-HCl, 1% SDS, 100 mM ME (β-mercaptoethanol).

SDS-PAGE and transfer, proteinase K treatment, RNA isolation, and cDNA library preparation

Eluted RNA-protein complexes were resolved on a 4%–12% Bis-Tris NuPAGE gel (Life Technologies) then transferred to a nitrocellulose membrane (GE Healthcare, Amersham Hybond ECL). The membrane was exposed on film (Amersham) at -70°C. The radioactive bands corresponding to the EZH2-RNA complexes were cut out, and then incubated with 150 μg of proteinase K (0.1 μg/mL final, QIAGEN, no. 19131) for 2 h at 55°C. The RNA was extracted with a phenol-chloroform-isoamyl alcohol mixture and ethanol precipitated overnight. The isolated RNA was reverse transcribed using miRCat-33 primer (IDT) with Superscript III Reverse Transcriptase (Life Technologies) and RNA was then degraded by addition of RNase H (NEB) for 30 min. cDNA was amplified using primers P5 and primer PE_miRCat_PCR and TaKaRa LA Taq polymerase (Takara Bio). RT was carried out with RT primer miRCat-33 primer (IDT) CCTTGGCACCCGAGAATT. Then we carried out 21 cycles of PCR (PE_miRCat_PCR) with the following PCR primers:

P5 AATGATACGGCGACCACCGAGATCTACACTCTTTCCCTACACGACGCTCTTCCGATCT.

PE_mircat_reverse CAAGCAGAAGACGGCATACGAGATCGGTCTCGGCATTCCTGGCCTTGGCACCCGAGAATTCC.

The product was gel purified, and samples pooled before submitting for sequencing. In total 20 μL of 3 ng/μL mixed sample was sent for sequencing with ∼0.3 ng/μL of each individual sample. Barcoded cDNA libraries from each sample were pulled together and subject

to high-throughput Illumina sequencing (PE100) at Bejing Genomics Institute (BGI).

The final library was of the following form:

5′-AATGATACGGCGACCACCGAGATCTACACTCTTTCCCTACACGACGCTCTTCCGATCT = = = INSERT = = = TGGAATTCTCGGGTGCCAAGGCCAGGAATGCCGAGACCGATCTCGTATGCCGTCTTCTGCTTG-3'.

FLASH-seq data processing

The raw sequenced reads were obtained in fastq format, and miRCat linker sequences were trimmed from the paired end data using cutadapt v.1.15 (https://github.com/marcelm/cutadapt [51]). The first read in each pair was retained for downstream analysis. Duplicate reads caused by PCR amplification were removed using the pyFastqDuplicateRemover.py tool from the pyCRAC suite,[52] and the remaining reads were aligned to the human genome (hg38) using Novoalign 2.07.[53] Overlaps between aligned reads and genomic features were calculated using the pyReadCounters.py tool from the pyCRAC suite, which also generated strand-specific overlap counts for each RNA biotype.

Differential binding was calculated using DESeq2[54] and differential enrichment for each transcript was determined by comparing EZH2 pull-down with IgG control, and against a known RNA binding protein hnRNPAB.[55] Comparable data were obtained from two independent biological replicates of primary ECs (Table S1) confirming that FLASH, with its stringent purification steps, is a robust method to identify endothelial RNA species and base pairing interactions with EZH2. The RNA-RNA hybrids were identified using a published hyb pipeline,[56] and MEG3 hybrid fragment sequences were extracted using hybtools.[57] The outputs of the hyb pipeline included a file with coordinates of all the hybrids ("*.hyb*") and a file with the folding analysis in "*.Viennad*" format. These and other output file formats are described in the hyb pipeline documentation, see https://github.com/gkudla/hyb. The stability of the predicted base pairing between the two RNA molecules in the chimeras was calculated as the change in free energy of hybridization (ΔG in kcal/mol), and hybrids with a ΔG value below −10 were retained. A total of 553 interactions passed this filtering step. Motif analysis was done using pyMotif.py from the pyCRAC suite. Enriched motifs in hybrid sequences and in the sequences of FLASH single-hit clusters were identified using MEME[52] https://meme-suite.org/meme/. Motif logos and E values (statistical significance from MEME) were obtained for top significant k-mers (4–8 nt in length).[58] These single-hit clusters were obtained by merging the genomic co-ordinates of overlapping reads using the pyClusterReads.py tool from the pyCRAC suite,[52] and then extracting their sequences from the complete human genome sequence using the bedtools getfasta command.[59] We also associated lncRNAs (annotated and unannotated) to the neighboring genes.

UV-RIP

HUVECs (2×10^6 cells per plate) were harvested from two 15-cm tissue culture plates following UV crosslinking as described above. The crosslinked pellet was lysed in ice-cold RIPA Lysis buffer (pH 8.0) (1 mL/pellet) (50 mM Tris [pH 8.0], 150 mM KCl, 0.1% SDS, 1% Triton X-100, 5 mM EDTA, 0.5% sodium deoxycholate) with addition of the following (per 1 mL): 100 U/mL RNAseOUT, 0.5 mM DTT, and 1× PIC as per suppliers' instructions and rotated for 30 min at 4°C. Resuspended lysates were sonicated as described above and supernatant collected following a spin in a microcentrifuge (16,000 rpm, 20 min, 4°C). To pre-clear the lysates, 25 μL of Protein G Dyneabeads (Life Technologies, 10003D) were added per immunoprecipitation condition for 30 min at 4°C, then removed. At this stage, we removed a 10 μL aliquot for RNA INPUT. Immunoprecipitation with pre-cleared UV-crosslinked lysates of ECs proceeded overnight at 4°C using antibodies against repressive chromatin (EZH2 [5246S] and H3K27me3 [9733S]) (see Table S11), IgG, or mock control (no antibody, hnRPAB), as described for ChIP. Beads were captured on a DynaMag magnet (Thermo Fisher Scientific, 12321D) and washed in 500 μL ice-cold Native Lysis buffer (150 mM KCl, 25 mM Tris [pH 7.5], 5 mM EDTA, 0.5% NP-40 with fresh addition of 0.5 mM DTT, 1× PIC, 100 U/mL RNaseOUT) to wash off the unbound material. Three RIP washes were performed at 4°C and beads pelleted (2,500 rpm, 30 s), followed by a final wash of 500 μL with Tris EDTA (10 mM Tris-HCl [pH 7.5]/1 mM EDTA). The beads or input samples were then resuspended in TRIzol (1 mL) vortexed vigorously for 10 s and incubated at room temperature for 10 min. Samples were usually stored at -80°C before further RNA extraction using a Monarch kit (NEB, no. T2010) following the manufacturer's instructions. RNA was eluted with nuclease-free water (e.g., 20 μL), quantified, and used in qPCR analysis, which was performed in triplicate.

Sonication of chromatin

UV-crosslinked lysates from FLASH and RIP were sonicated (6 × 2 min ON/30 s OFF) to fragment DNA to 200–700 bp, and centrifuged (15 min) using a Bioruptor sonicator (Diagenode). Glutaraldehyde crosslinked (1%) lysates from ChIRP were sonicated on a Covaris E220 Evolution Focused-Ultrasonicator System using a water at a temperature range of 5°C-7°C and the following protocol: peak power 140 W, duty factor 10%, 200 cycles per burst for 60 s. A total of 30–35 cycles was used for cell lysates prepared from 150 mg of crosslinked HUVEC pellets. Samples were then centrifuged (16,000 rcf, 15 min at 4°C) and 10 μL supernatant was removed from each condition for DNA isolation following de-crosslinking. DNA was eluted by adding 150 μL elution buffer and shaking (37°C, 30 min, 900 rpm) and 15 μL proteinase K (10 mg/mL, Sigma, P4850) was added per sample and shaking repeated (50°C, 45min, 900 rpm). DNA was purified using a QIAquick PCR Purification Kit. Fragment size was determined by resolving samples on 1.5% agarose gel with 1-kb and 100-bp ladders for reference. The gel was imaged, and fragments visualized using a UVidoc HD6 system (UVitec).

ChIRP was performed as described previously[60] using two sets of biotin-labeled antisense oligonucleotide DNA probes targeting MEG3, whereas biotinylated LacZ probes served as negative controls. We used published probes and designed additional ones at http://www.singlemoleculefish.com/designer.html and validated them.

Sequences of MEG3 and LacZ control probes and non-biotinylated control probes are reported in Table S10. 3′-Biotinylated antisense MEG3 DNA oligonucleotide probes were incubated with chromatin lysates from HUVECs. Before, cells were fixed with 1% glutaraldehyde (Sigma-Aldrich) and the crosslinking reaction was quenched with glycine (0.125 mM). The crosslinked cells were pelleted (>100 mg) and stored at -80°C until use. Next, 100–150 mg pellets were pulverized in liquid nitrogen and chromatin prepared as reported before.[61] Lysate/sample (1%) condition was saved as input and 10%/90% samples were used for RNA/DNA extraction, respectively. Chromatin complexes were purified using RNA pull-down with streptavidin-labeled C-1 magnetic beads (Invitrogen, 65001). Subsequent stringent washes of beads:biotin-probes:RNA:chromatin were performed as described previously.[62] MEG3-bound DNA and proteins were eluted off the beads using nuclear hybridization buffer (0.75 M NaCl, 50 mM Tris-HCl [pH 7.0], 1 mM EDTA, 1% SDS, 15% formamide and water, with 1 mM AEBSF, 0.01× vol protease inhibitor cocktail [Sigma P8340]) and 0.01× vol RNase inhibitor [Sigma R1158] added fresh just before use) and incubated for 60 min at 37°C. After the incubation, beads were collected and washed four times with 500 mL of ChIRP wash buffer (2× SSC, 0.5% SDS, and fresh 1 mM AEBSF and 0.01× vol RNA inhibitor added). After the last wash, beads were deposed in elution buffer (50 mM $NaHCO_3$, 1% SDS, 200 mM NaCl) with 10 μL of proteinase K (10 mg/mL, Sigma P4850), and reversal of crosslinking was performed at 65°C for 3 h. DNA was eluted with a cocktail of 100 mg/mL RNase A (Sigma-Aldrich) and 0.1 U/mL RNase H (Ambion) and recovered using a Monarch kit (T1030L) and used for library construction. RNA was TRIzol-extracted and purified. The quality and RNA was assessed using an Agilent RNA 6000 Pico Kit and an Agilent Bioanalyser, obtaining the quantification information. A Qubit High Sensitivity DNA Kit (Life Technologies, Q32851) was used to obtain total DNA concentration and DNA peak distribution and fragments of DNA 1000 allowing a correct sizing and quantification analysis. The input and odd and even probes samples were sequenced individually.

ChIRP-seq data processing

Biotin-labeled probes targeting MEG3:RNA and MEG3:DNA complexes (Figure 3A) were captured with streptavidin magnetic beads as reported before.[63] The specificity of biotin-labeled probes for MEG3 gene, as opposed to other genes, was confirmed using one-step qPCR with RNA purified from ChIRP (Figure 3B). Initial processing and alignment of sequenced ChIRP-seq data was performed by at BGI, where initial fastq filtering using SOAPnuke was performed.[64] Filtered reads were aligned to the human genome (hg38) using bwa 0.7.15, and peaks called using MACS2 v.2.2.7.1.[65] The code for processing the aligned ChIRP-seq data is given here: https://github.com/hyweldd/2024_mtna_chirpseq_pipeline. Genomic coverage of ChIRP-seq peaks was calculated using bedtools merge[59] and bedGraphToBigWig[66] as outlined in Figure S3D. Profiles and heatmaps around the TSS of mRNAs were created using the computeMatrix, plotHeatmap, and plotProfile tools from the deepTools suite.[67] Identified genomic sites of MEG3 interactions were considered as true MEG3-targets if they were recognized in both independent ChIRP experiments and in the RNA-seq experiments as bellow and undetected in the negative ChIRP control (using probes against *LacZ* RNA) (Table S10).

ChIP

ChIP assays were performed essentially as described previously.[8] In brief, chromatin in control and treated cells (1×10^7) were crosslinked with 1% formaldehyde solution (methanol-free, Thermo Fisher Scientific) at a volume of 0.5 mL for every 1×10^6 cell for 10 min at room temperature with slow rotation. Fixation was quenched using glycine (125 mM, 5 min) followed by 3× PBS washes. Cells were collected and incubated in lysis buffer (150 mM NaCl, 25 mM Tris [pH 7.5], 1% Triton X-100, 0.1% SDS, 0.5% deoxycholate) supplemented with a protease inhibitor tablet and PMSF. DNA was fragmented into 200–700-bp pieces using a chilling Bioruptor sonicator (6 × 2 min ON/30 s OFF/30 s, 4°C) and lysates centrifuged (15 min, 1,000 rcf, 4°C). Aliquots of lysates containing 200 μg of protein were used for each immunoprecipitation reaction with EZH2 (D2C9) XP(R) rabbit mAb (Cell Signaling Technology, 5246S), tri-methyl-histone H3 (H3K27me3) (C36B11) rabbit mAb (9733S, CST) antibodies, or IgG control (normal rabbit IgG, CST, 2729S) and captured on beads using Protein G Dynabeads (Life Technologies, 10003D). The immune complexes were eluted with the elution buffer (1% SDS, 100 mM $NaCO_3$) supplemented with proteinase K (10 μg/mL) and with shaking at 65°C, 1,000 rpm for 3–6 h. DNA was purified using a Monarch kit (T1030L).

ChIP followed by sequencing or qPCR after MEG3 KD

We immunoprecipitated EZH2, together with associated chromatin isolated from the HUVECs (2×10^6) previously transfected with MEG3 GapmeRs (10 nM, 48 h) or a scrambled control GapmeRs (control) and purified bound DNA for sequencing or analysis by qPCR. For transfection, we used 10 nM scrambled LNA (locked nucleic acids) GapmeR control (cat. no. 339515) or phosphorothioate antisense standard GapmeRs MEG3-lncRNA (QIAGEN, cat. no. 339511). On beads, crosslinked chromatin complexes were reversed, and DNA purified using a QIAquick PCR Purification Kit and quantified using a Qubit HS assay (Q33230) following the manufacturer's instructions. The comparative delta Ct value method was used for qPCR analysis with positive and negative primer controls to validate the binding. Prior to sending for sequencing, DNA quality and concentration was measured using an Agilent HS DNA kit (5067-4626).

Overlap between ChIRP targets and EZH2-binding sites

ChIP-seq extracted bed files of histone mark H3K27me3 were downloaded from GEO GSM733688 and GSM945180. The bed files for the public ChIP-seq database for epigenetic regulator EZH2 in HUVECs were downloaded from GEO accession number GSE109626. ChIP-seq peaks in bed format were lifted over from hg19 to hg38 using liftOver[66] and concatenated. GEO datasets in the NCBI portal (ncbi.nlm.nih.gov) were searched using the key words "EZH2" or "H3K27me3 ChIP-seq in HUVECs." All intersections with called peaks from ChIP-seq data obtained from GEO were calculated using the bedtools intersect command.[59] All bed intersections of extracted peaks between ChIP-seq and ChIRP-seq were calculated using the

bedtools intersect command.[59] Maximum peak scores for ChIRP-seq peaks that overlap genomic features were calculated using bedmap from the bedops suite (https://bedops.readthedocs.io/en/latest/).[68] The ChIP enrichment profiles were also compared with the LacZ ChIRP controls. Functional profiling of overlaping ChIRP and ChIP targets with maximum peak scores, is reported in Table 1.

RNA-seq processing following MEG3 KD in HUVECs

HUVECs were seeded onto 6-well plates and transfected with LNA GapmeRs against MEG3 (10 nM, QIAGEN) as described above, by incubation (6 h, 37°C, 5% CO_2), then complexes and Optimem were replaced with medium for a further 48 h. RNA was collected and purified before quantification ahead of sequencing using BGI services. RNA-seq analyses of control (n=4) and MEG3-depleted RNA (n = 3/group) were performed in-house. Raw fastq files were processed using the nf-core RNA-seq pipeline release 3.12.0 (https://github.com/nf-core/rnaseq/tree/3.12.0), using Salmon for quantification, and hg38 as the reference genome assembly. Differential expression analysis was performed using DESeq2,[54] and plots were generated in R. The differential expression analysis was performed using three biological replicates of the MEG3 KD experiment and four controls.

De novo analysis of RNA-seq data

Raw SRA files of RNA-seq data were obtained from GEO GSE71164, converted to FASTQ files, and aligned using TopHat2 (v.2.0.3).[69] *De novo* analyses were performed and data aligned to human genome build Hg38 via STAR[70] and DESeq2,[54] using a human genome database from Ensembl release 77 (www.ensembl.org). GTF (gene transfer format) files were generated as described before.[71] Statistical analysis of the differential expression of genes was performed using EdgeR. Genes with false discovery rate for differential expression lower than 0.01 were considered significant.

Pharmacological inhibition of PRC2

The solution of A-395 inhibitor (Sigma, SML1923) was prepared as per the manufacturer's instructions. A-395 is a potent chemical probe that binds to the H3K27me3 binding pocket of EED to allosterically inhibit and disrupt the trimeric PRC2 protein complex.[72] For *in vitro* assays it was used at 5 μM final concentration with 0.01% DMSO in water from the 50 μM stock, whereas for *in vivo* studies the final dose was 10 mg/kg (i.p.). The working stock concentration was 2 mg/mL, used from a stock of 100 mg/mL dissolved in water (vehicle). Working stock was stored at 4°C and aliquoted stock solutions were kept at -20°C until needed for experiment.

Immunocytochemistry

HUVECs (2×10^6) were transfected with MEG3 GapmeRs (10 nM, 48 h) or a scrambled control GapmeRs (control), or treated with A-395 inhibitor (Sigma, SML1923; 5 μM final) with 0.01% DMSO in water, diluted from 50 μM stock. Methanol-ethanol fixation was prepared in a 1:1 methanol and ethanol mixture and cells fixed at -20°C for 5-10 min. Cell staining was performed following the manufacturer's instructions for ITGA4 and isotype control antibody, as reported in Table S11.

Fluorescent *in situ* hybridization against MEG3 transcript

Custom Stellaris fluorescent *in situ* hybridization (FISH) Probes recognizing MEG3 and labeled with Cy3 were purchased from Biosearch Technologies (https://www.biosearchtech.com/; Petaluma, CA). The HUVECs were hybridized with the MEG3 Stellaris FISH Probe set, following the manufacturer's instructions available online at www.biosearchtech.com/stellarisprotocols.

In brief, cells were incubated with hybridization buffer (50% formamide, 4× SSC, 2.5× Denhadrt's solution, 2.5 mg/mL salmon DNA, 0.6 mg/mL yeast tRNA, 0.025% SDS, and 0.1% blocking reagent) at 37°C for 1 h followed by a 37°C overnight incubation with 125 nM of MEG3 probes conjugated with Cy3 in the same buffer. Detection of EZH2 (Cell Signaling; [D2C9] XP rabbit mAb no. 5246; 1:100) was subsequently performed and detected using Alexa Fluor 488 (Thermo Fisher Scientific, 1:500) secondary antibody using a Zeiss fluorescent microscope.

Protein quantification by western blot analysis

Protein samples were prepared from cells using a lysis buffer containing a protease inhibitor (Roche, 11852700) and phosphatase inhibitor (Thermo Fisher Scientific, 88667). Protein lysates were matched for protein concentration; total protein (15 μg) was resolved by SDS-PAGE and transferred onto PVDF membranes (Bio-Rad) that were incubated with integrin ITGA4 primary antibody and revealed with appropriate HRP-linked secondary antibody (Table S9). Densities of the immunoreactive bands were evaluated using NIH ImageJ software. Protein loading was verified against β-actin densities.

In vitro functional studies

HUVECs were pre-treated with A-395 (5 μM) in 12-well plates for 24 h or transfected with siRNA for *ITGA4* (20 nM, Thermo Fisher Scientific). ECs were plated in a FN-coated (20 μg/mL) 8W10E$^+$ electrode chamber array. Cell adhesion was continuously recorded for a further 7 h using an ECIS Z-Theta system (Applied Biophysics) with associated software as reported before[73] and then resistance changes were calculated. Migration was analyzed using an ECIS chip array (8W1E) coated in a FN-gelatin coating mix (1 μg/mL FN/0.01% gelatin) as reported by us previously.[74] The migration speed was calculated in micrometers per hour.

Statistical analysis

Unless otherwise stated each experiment was performed three times (biological replicates). All statistical comparisons between two groups or multiple groups were performed using GraphPad Prism 10.2.1 (171) software. Normally distributed variables were compared between groups using Student's *t*-test and *p* values were calculated. Two-way analysis or ANOVA test was performed followed by Bonferroni post hoc test or Dunnett's correction as indicated in the figure legends. Statistical significance was determined when $p \leq 0.05$, and $p > 0.05$ was not significant. If not alternatively specified, all error

bars represent mean values with SEM. Permutation tests with asymptotic approximation were performed in R using the Perm R-package run in R.[75]

Data processing and software analysis

The gene-type distribution of reads was revealed using *Pavis* online software, PAVIS[76] and all gene ID crosses in the study were done using JVenn.[77] GO pathway analysis was performed on determined protein-coding genes, using Panther Pathways,[78] g:Profiler (v.0.6.7),[79] and Enrichr.[80,81] The g:Profiler database Ensembl 103, Ensembl Genomes 50 (build date 2021-04-14) was used. Only GO terms with $p < 0.05$ were used for further analysis. The list of mouse protein-coding genes was converted to human orthologous gene IDs that were obtained using g:Orth https://biit.cs.ut.ee/gprofiler/orth or converted using https://biit.cs.ut.ee/gprofiler/convert, and used in downstream representation. The python pyCRAC v.1.5.2[52] software package was used for analyzing the data, available from ECDF Gitlab repository https://git.ecdf.ed.ac.uk.

DATA AND CODE AVAILABILITY

All sequence data from this study, Genome maps, Bedgraph, and GTF files generated from the analysis of the Hfq FLASH (GSE230112), ChIRP-seq (GSE234542), ChIP-seq (GSE234543), or RNA-seq (GSE253830) have been deposited into the GEO. Re-mapped RNA-seq data of the GEO dataset GSE71164 are available from University of Edinburgh Data repository at https://bifx-core3.bio.ed.ac.uk/hyweldd/tmitic. All other data underlying the key findings are available in the supplemental information. All computational analysis processing pipelines are available from https://github.com/hyweldd. The *hyb* pipeline for identifying chimeric reads and the hybtools package for downstream identification of first read in a pair are available at https://github.com/gkudla/hyb. All doppler imaging scans, blood flow ratios and data analysis from animal study are available at "Zenodo: https://zenodo.org/records/10902595".

ChIP-seq-extracted bed files of histone mark H3K27me3 for chromatin state in motor neurons were downloaded from GSE114283. Peaks unique to control vs. *MEG3* KD were assigned to positions associated with promoters and gene lists that were obtained from Ensembl Biomart, geneset v.97 with added 2,000 bp upstream.[82] Gene region list was submitted to GREAT (Genomic Regions Enrichment of Annotations Tool) to compose associated mouse gene list.[83] DAVID enrichment tool and clustering were used[84] and the computational analysis pipeline is described as outlined in Figure S4B.

RNA-seq *de novo* mapping and analysis employed RNA sequences extracted from the GEO dataset GSE71164 and is available in Table S9. The microarray dataset from identification of differentially expressed genes in murine C2C12 cell lines after MEG3 KD was extracted from the GSE73524 dataset. Using GEO2R, two or more groups were assigned and compared (control vs. *MEG3* KD) to obtain the top differentially expressed genes as instructed https://www.ncbi.nlm.nih.gov/geo/info/geo2r.html#how_to_use.[85] A list of identified mouse targets and human ortholog genes was obtained upon data processing and is given in Table S10.

SUPPLEMENTAL INFORMATION

Supplemental information can be found online at https://doi.org/10.1016/j.omtn.2024.102173.

ACKNOWLEDGMENTS

This work was supported by the British Hearth Foundation (BHF) Career Re-entry Fellowship (FS/16/38/32351), Wellcome Trust Institutional Strategic Funding Award (IS3-R1.12 19/20), and the BHF REA3 Institutional Award (RE/18/5/34216) (to T.M.). We are grateful for the support by BHF project grant (RG/20/5/34796) (to J.R.) and Cardioregenix grant (825670) (to T.D.). H.D.-D. was supported by the Core grant (092076) to the Wellcome Centre for Cell Biology at the University of Edinburgh. A.M. and P.G. are funded by the UK Medical Research Council (MRC core funding of the MRC Human Genetics Unit). D.T. was supported by the Wellcome Trust (109916, 222516). A.B. is supported by the BHF personal Chair (CH/11/2/28733). Furthermore, we thank the IGMM Mass Spectrometry Facility and Wellcome Trust Clinical Research Fascility in Edinburgh for processing the samples, and Alex von Kriegsheim for support with designing proteomics experiments, Richard Clark for help with sonicating samples, rispectively; Pam Holland for technical support. Finally, we are grateful to Dr. Mark Miller, Prof. Dave Newby, Dr. Rob Illingworth, and Prof. Alejandra San Martin for their fruitful discussions and valuable feedback on the project and for critically reading the manuscript. The graphical abstract and Figure 1B were created using Biorender.com.

AUTHOR CONTRIBUTIONS

T.M. is the senior author of this work responsible for the conception, study design, funding acquisition, and project administration (including resources, experimental investigation, data collection and analysis). T.M. wrote the manuscript, revised drafts, handled re-submissions, and drew the graphical abstract. H.D.-D. performed substantial bioinformatics work, data curation, wrote pipelines for analyses, and managed, annotated, and maintained raw data. T.D. performed FLASH experiments and prepared the library for sequencing. A.N. performed ChIRP experiments, molecular biology, *in vitro* and *ex vivo* experiments and analyses. E.P. performed fluorescent staining. A.C. provided essential equipment and infrastructure for imagining analyses. A.C.T. performed *in vivo* experiments and analyzed the data. P.M. contributed to analysis of *in vivo* data. P.G., A.M., I.U., and J.R. contributed to bioinformatic data analyses. I.U. advised on processing ChIRP-seq data, and steps for the processing pipeline. T.M., A.C., A.B., D.T., and P.M. advised on experimental design and provided essential equipment and infrastructure. T.M., H.D.-D., D.T., T.D., and A.B. contributed with resources, advised on experimental design, data processing and analysis, or contributed to manuscript editing and discussions.

DECLARATION OF INTERESTS

The authors declare no competing interests.

DECLARATION OF GENERATIVE AI AND AI-ASSISTED TECHNOLOGIES IN THE WRITING PROCESS

During the preparation of this work the authors used Grammarly AI writing assistant to improve readability and correct spelling of the manuscript. After using this tool/service, the authors reviewed and edited the content as needed and take full responsibility for the content of the publication.

REFERENCES

1. Rosa-Garrido, M., Chapski, D.J., and Vondriska, T.M. (2018). Epigenomes in Cardiovascular Disease. Circ. Res. *122*, 1586–1607.
2. Batie, M., Frost, J., Frost, M., Wilson, J.W., Schofield, P., and Rocha, S. (2019). Hypoxia induces rapid changes to histone methylation and reprograms chromatin. Science *363*, 1222–1226.
3. Trotman, J.B., Braceros, K.C.A., Cherney, R.E., Murvin, M.M., and Calabrese, J.M. (2021). The Control of Polycomb Repressive Complexes by Long Noncoding RNAs. Wiley Interdiscip. Rev. RNA *12*, e1657.
4. Yuan, J.-L., Yin, C.-Y., Li, Y.-Z., Song, S., Fang, G.-J., and Wang, Q.-S. (2021). EZH2 as an Epigenetic Regulator of Cardiovascular Development and Diseases. J. Cardiovasc. Pharmacol. *78*, 192–201.
5. Rosenberg, M., Blum, R., Kesner, B., Aeby, E., Garant, J.M., Szanto, A., and Lee, J.T. (2021). Motif-driven interactions between RNA and PRC2 are rheostats that regulate transcription elongation. Nat. Struct. Mol. Biol. *28*, 103–117.
6. Blackledge, N.P., and Klose, R.J. (2021). The molecular principles of gene regulation by Polycomb repressive complexes. Nat. Rev. Mol. Cell Biol. *22*, 815–833.
7. Tang, Y., Zhao, L., Yu, X., Zhang, J., Qian, L., Jin, J., Lu, R., and Zhou, Y. (2021). Inhibition of EZH2 primes the cardiac gene activation via removal of epigenetic repression during human direct cardiac reprogramming. Stem Cell Res. *53*, 102365.
8. Mitić, T., Caporali, A., Floris, I., Meloni, M., Marchetti, M., Urrutia, R., Angelini, G.D., and Emanueli, C. (2015). EZH2 Modulates Angiogenesis *In Vitro* and in a Mouse Model of Limb Ischemia. Mol. Ther. *23*, 32–42.
9. Lino Cardenas, C.L., Kessinger, C.W., MacDonald, C., Jassar, A.S., Isselbacher, E.M., Jaffer, F.A., and Lindsay, M.E. (2018). Inhibition of the methyltranferase EZH2 improves aortic performance in experimental thoracic aortic aneurysm. JCI Insight *3*, e97493.
10. Colón-Caraballo, M., Torres-Reverón, A., Soto-Vargas, J.L., Young, S.L., Lessey, B., Mendoza, A., Urrutia, R., and Flores, I. (2018). Effects of histone methyltransferase inhibition in endometriosis. Biol. Reprod. *99*, 293–307.
11. Wang, J., and Wang, G.G. (2020). No Easy Way Out for EZH2: Its Pleiotropic, Noncanonical Effects on Gene Regulation and Cellular Function. Int. J. Mol. Sci. *21*, 9501.
12. Yuan, J.L., Yin, C.Y., Li, Y.Z., Song, S., Fang, G.J., and Wang, Q.S. (2021). EZH2 as an epigenetic regulator of cardiovascular development and diseases. J. Cardiovasc. Pharmacol. *78*, 192–201.
13. Sherpa, C., Rausch, J.W., and Le Grice, S.F. (2018). Structural characterization of maternally expressed gene 3 RNA reveals conserved motifs and potential sites of interaction with polycomb repressive complex 2. Nucleic Acids Res. *46*, 10432–10447.
14. Gordon, F.E., Nutt, C.L., Cheunsuchon, P., Nakayama, Y., Provencher, K.A., Rice, K.A., Zhou, Y., Zhang, X., and Klibanski, A. (2010). Increased expression of angiogenic genes in the brains of mouse meg3-null embryos. Endocrinology *151*, 2443–2452.
15. He, C., Yang, W., Yang, J., Ding, J., Li, S., Wu, H., Zhou, F., Jiang, Y., Teng, L., and Yang, J. (2017). Long Noncoding RNA MEG3 Negatively Regulates Proliferation and Angiogenesis in Vascular Endothelial Cells. DNA Cell Biol. *36*, 475–481.
16. Boon, R.A., Hofmann, P., Michalik, K.M., Lozano-Vidal, N., Berghäuser, D., Fischer, A., Knau, A., Jaé, N., Schürmann, C., and Dimmeler, S. (2016). Long Noncoding RNA Meg3 Controls Endothelial Cell Aging and Function. J. Am. Coll. Cardiol. *68*, 2589–2591.
17. Xing, Y., Zheng, X., Fu, Y., Qi, J., Li, M., Ma, M., Wang, S., Li, S., and Zhu, D. (2019). Long Noncoding RNA-Maternally Expressed Gene 3 Contributes to Hypoxic Pulmonary Hypertension. Mol. Ther. *27*, 2166–2181.
18. Li, X., Zhao, J., Geng, J., Chen, F., Wei, Z., Liu, C., Zhang, X., Li, Q., Zhang, J., Gao, L., et al. (2019). Long non-coding RNA MEG3 knockdown attenuates endoplasmic reticulum stress-mediated apoptosis by targeting p53 following myocardial infarction. J. Cell Mol. Med. *23*, 8369–8380.
19. Helwak, A., and Tollervey, D. (2016). Identification of miRNA-Target RNA Interactions Using CLASH. Methods Mol. Biol. *1358*, 229–251.
20. Iosub, I.A., van Nues, R.W., McKellar, S.W., Nieken, K.J., Marchioretto, M., Sy, B., Tree, J.J., Viero, G., and Granneman, S. (2020). Hfq CLASH uncovers sRNA-target interaction networks linked to nutrient availability adaptation. Elife *9*, e54655.
21. Bharathavikru, R., Dudnakova, T., Aitken, S., Slight, J., Artibani, M., Hohenstein, P., Tollervey, D., and Hastie, N. (2017). Transcription factor Wilms' tumor 1 regulates developmental RNAs through 3' UTR interaction. Genes Dev. *31*, 347–352.
22. Beltran, M., Yates, C.M., Skalska, L., Dawson, M., Reis, F.P., Viiri, K., Fisher, C.L., Sibley, C.R., Foster, B.M., Bartke, T., et al. (2016). The interaction of PRC2 with RNA or chromatin is mutually antagonistic. Genome Res. *26*, 896–907.
23. Thompson, J.D., Higgins, D.G., and Gibson, T.J. (1994). CLUSTAL W: improving the sensitivity of progressive multiple sequence alignment through sequence weighting, position-specific gap penalties and weight matrix choice. Nucleic Acids Res. *22*, 4673–4680.
24. Yates, A., Akanni, W., Amode, M.R., Barrell, D., Billis, K., Carvalho-Silva, D., Cummins, C., Clapham, P., Fitzgerald, S., Gil, L., et al. (2016). Ensembl 2016. Nucleic Acids Res. *44*, D710–D716.
25. Mi, H., Muruganujan, A., Huang, X., Ebert, D., Mills, C., Guo, X., and Thomas, P.D. (2019). Protocol Update for large-scale genome and gene function analysis with the PANTHER classification system (v.14.0). Nat. Protoc. *14*, 703–721.
26. Dunn-Davies, H., Dudnakova, T., Baker, A.H., and Mitić, T. (2024). Epigenetic control of vascular endothelial function revealed by multi-omics. Eur. Heart J. *45*, 642–644.
27. Yan, J., Dutta, B., Hee, Y.T., and Chng, W.J. (2019). Towards understanding of PRC2 binding to RNA. RNA Biol. *16*, 176–184.
28. Jadhav, U., Nalapareddy, K., Saxena, M., O'Neill, N.K., Pinello, L., Yuan, G.-C., Orkin, S.H., and Shivdasani, R.A. (2016). Acquired Tissue-Specific Promoter Bivalency Is a Basis for PRC2 Necessity in Adult Cells. Cell *165*, 1389–1400.
29. Gunawan, M., Venkatesan, N., Loh, J.T., Wong, J.F., Berger, H., Neo, W.H., Li, L.Y.J., La Win, M.K., Yau, Y.H., Guo, T., et al. (2015). The methyltransferase Ezh2 controls cell adhesion and migration through direct methylation of the extranuclear regulatory protein talin. Nat. Immunol. *16*, 505–516.
30. Dill, T.L., Carroll, A., Gao, J., and Naya, F.J. (2020). The long noncoding RNA Meg3 regulates myoblast plasticity and muscle regeneration through epithelial-mesenchymal transition. Preprint at bioRxiv. https://doi.org/10.1101/2020.06.15.152884.
31. Naya, F., Dill, T., Carroll, A., Pinheiro, A., and Gao, J. (2020). Transcriptomic Data and Analyses of shMeg3 Muscle *in Vitro* and *in Vivo*.
32. Hsu, J.H.R., Rasmusson, T., Robinson, J., Pachl, F., Read, J., Kawatkar, S., O' Donovan, D.H., Bagal, S., Code, E., Rawlins, P., et al. (2020). EED-Targeted PROTACs Degrade EED, EZH2, and SUZ12 in the PRC2 Complex. Cell Chem. Biol. *27*, 41–46.e17.
33. (2017). Targeting the EED–H3K27me3 Interaction Allosterically Inhibits PRC2. Cancer Discov. *7*, OF8.
34. Bachman, H., Nicosia, J., Dysart, M., and Barker, T.H. (2015). Utilizing Fibronectin Integrin-Binding Specificity to Control Cellular Responses. Adv. Wound Care *4*, 501–511.
35. Mezu-Ndubuisi, O.J., and Maheshwari, A. (2021). The role of integrins in inflammation and angiogenesis. Pediatr. Res. *89*, 1619–1626.
36. Uroda, T., Anastasakou, E., Rossi, A., Teulon, J.M., Pellequer, J.L., Annibale, P., Pessey, O., Inga, A., Chillón, I., and Marcia, M. (2019). Conserved Pseudoknots in lncRNA MEG3 Are Essential for Stimulation of the p53 Pathway. Mol. Cell *75*, 982–995.e9.
37. Wang, X., Goodrich, K.J., Gooding, A.R., Naeem, H., Archer, S., Paucek, R.D., Youmans, D.T., Cech, T.R., and Davidovich, C. (2017). Targeting of Polycomb Repressive Complex 2 to RNA by Short Repeats of Consecutive Guanines. Mol. Cell *65*, 1056–1067.e5.

38. LaFlamme, S.E., Mathew-Steiner, S., Singh, N., Colello-Borges, D., and Nieves, B. (2018). Integrin and microtubule crosstalk in the regulation of cellular processes. Cell. Mol. Life Sci. *75*, 4177–4185.

39. Mostafavi-Pour, Z., Askari, J.A., Parkinson, S.J., Parker, P.J., Ng, T.T.C., and Humphries, M.J. (2003). Integrin-specific signaling pathways controlling focal adhesion formation and cell migration. J. Cell Biol. *161*, 155–167.

40. Calzada, M.J., Zhou, L., Sipes, J.M., Zhang, J., Krutzsch, H.C., Iruela-Arispe, M.L., Annis, D.S., Mosher, D.F., and Roberts, D.D. (2004). Alpha4beta1 integrin mediates selective endothelial cell responses to thrombospondins 1 and 2 *in vitro* and modulates angiogenesis *in vivo*. Circ. Res. *94*, 462–470.

41. Cai, W.-J., Li, M.B., Wu, X., Wu, S., Zhu, W., Chen, D., Luo, M., Eitenmüller, I., Kampmann, A., Schaper, J., and Schaper, W. (2009). Activation of the integrins α5β1 and αvβ3 and focal adhesion kinase (FAK) during arteriogenesis. Mol. Cell. Biochem. *322*, 161–169.

42. Henning, C., Branopolski, A., Schuler, D., Dimitroulis, D., Huelsemann, P., Nicolaus, C., Sansone, R., Ludolf Postma, J., Eberhard, D., Le Noble, F., et al. (2019). Requirement of β1 integrin for endothelium-dependent vasodilation and collateral formation in hindlimb ischemia. Sci. Rep. *9*, 16931.

43. Mondal, T., Subhash, S., Vaid, R., Enroth, S., Uday, S., Reinius, B., Mitra, S., Mohammed, A., James, A.R., Hoberg, E., et al. (2015). MEG3 long noncoding RNA regulates the TGF-[beta] pathway genes through formation of RNA-DNA triplex structures. Nat. Commun. *6*, 7743.

44. Warwick, T., Brandes, R.P., and Leisegang, M.S. (2023). Computational Methods to Study DNA:DNA:RNA Triplex Formation by lncRNAs. Noncoding. RNA *9*, 10.

45. Leisegang, M.S., Bains, J.K., Seredinski, S., Oo, J.A., Krause, N.M., Kuo, C.-C., Günther, S., Sentürk Cetin, N., Warwick, T., Cao, C., et al. (2022). HIF1α-AS1 is a DNA:DNA:RNA triplex-forming lncRNA interacting with the HUSH complex. Nat. Commun. *13*, 6563.

46. Kraft, K., Yost, K.E., Murphy, S.E., Magg, A., Long, Y., Corces, M.R., Granja, J.M., Wittler, L., Mundlos, S., Cech, T.R., et al. (2022). Polycomb-mediated genome architecture enables long-range spreading of H3K27 methylation. Proc. Natl. Acad. Sci. USA *119*, e2201883119.

47. Jenkins, W.S.A., Vesey, A.T., Stirrat, C., Connell, M., Lucatelli, C., Neale, A., Moles, C., Vickers, A., Fletcher, A., Pawade, T., et al. (2017). Cardiac $\alpha_V\beta_3$ integrin expression following acute myocardial infarction in humans. Heart *103*, 607–615.

48. Mayer, A., and Churchman, L.S. (2017). A Detailed Protocol for Subcellular RNA Sequencing (subRNA-seq). Curr. Protoc. Mol. Biol. *120*, 4.29.1–4.29.18.

49. Gagnon, K.T., Li, L., Janowski, B.A., and Corey, D.R. (2014). Analysis of nuclear RNA interference in human cells by subcellular fractionation and Argonaute loading. Nat. Protoc. *9*, 2045–2060.

50. Waters, S.A., McAteer, S.P., Kudla, G., Pang, I., Deshpande, N.P., Amos, T.G., Leong, K.W., Wilkins, M.R., Strugnell, R., Gally, D.L., et al. (2017). Small RNA interactome of pathogenic E. coli revealed through crosslinking of RNase E. EMBO J. *36*, 374–387.

51. Martin, M. (2011). Cutadapt removes adapter sequences from high-throughput sequencing reads. EMBnet. j. *17*, 10. *Next Generation Sequencing Data AnalysisDO*.

52. Webb, S., Hector, R.D., Kudla, G., and Granneman, S. (2014). PAR-CLIP data indicate that Nrd1-Nab3-dependent transcription termination regulates expression of hundreds of protein coding genes in yeast. Genome Biol. *15*, R8.

53. Novocraft Technologies (2021). Novocraft.

54. Love, M.I., Huber, W., and Anders, S. (2014). Moderated estimation of fold change and dispersion for RNA-seq data with DESeq2. Genome Biol. *15*, 550.

55. Kent, W.J., Zweig, A.S., Barber, G., Hinrichs, A.S., and Karolchik, D. (2010). BigWig and BigBed: enabling browsing of large distributed datasets. Bioinformatics *26*, 2204–2207.

56. Travis, A.J., Moody, J., Helwak, A., Tollervey, D., and Kudla, G. (2014). Hyb: A bioinformatics pipeline for the analysis of CLASH (crosslinking, ligation and sequencing of hybrids) data. Methods *65*, 263–273.

57. Dunn-Davies, H., Dudnakova, T., Langhendries, J.-L., Watkins, N., Lafontaine, D.L.J., and Tollervey, D. (2021). Systematic mapping of small nucleolar RNA targets in human cells. Preprint at bioRxiv. https://doi.org/10.1101/2021.07.22.451324.

58. Bailey, T.L., Johnson, J., Grant, C.E., and Noble, W.S. (2015). The MEME Suite. Nucleic Acids Res. *43*, W39–W49.

59. Quinlan, A.R., and Hall, I.M. (2010). BEDTools: a flexible suite of utilities for comparing genomic features. Bioinformatics *26*, 841–842.

60. Chu, C., and Chang, H.Y. (2016). Understanding RNA-Chromatin Interactions Using Chromatin Isolation by RNA Purification (ChIRP). Methods Mol. Biol. *1480*, 115–123.

61. Simon, J.M., Giresi, P.G., Davis, I.J., and Lieb, J.D. (2012). Using formaldehyde-assisted isolation of regulatory elements (FAIRE) to isolate active regulatory DNA. Nat. Protoc. *7*, 256–267.

62. Au - Chu, C., Au - Quinn, J., and Au - Chang, H.Y. (2012). Chromatin Isolation by RNA Purification (ChIRP). JoVE *25*, e3912.

63. Terashima, M., Tange, S., Ishimura, A., and Suzuki, T. (2017). MEG3 Long Noncoding RNA Contributes to the Epigenetic Regulation of Epithelial-Mesenchymal Transition in Lung Cancer Cell Lines. J. Biol. Chem. *292*, 82–99.

64. Chen, S., Zhou, Y., Chen, Y., and Gu, J. (2018). fastp: an ultra-fast all-in-one FASTQ preprocessor. Bioinformatics *34*, i884–i890.

65. Zhang, Y., Liu, T., Meyer, C.A., Eeckhoute, J., Johnson, D.S., Bernstein, B.E., Nusbaum, C., Myers, R.M., Brown, M., Li, W., and Liu, X.S. (2008). Model-based Analysis of ChIP-Seq (MACS). Genome Biol. *9*, R137.

66. Kuhn, R.M., Haussler, D., and Kent, W.J. (2013). The UCSC genome browser and associated tools. Brief. Bioinf. *14*, 144–161.

67. Ramírez, F., Ryan, D.P., Björn, G., Vivek, B., Fabian, K., Andreas, S.R., Steffen, H., Friederike, D., and Thomas, M. (2016). deepTools2: a next generation web server for deep-sequencing data analysis. Nucleic Acids Res. *44*, gkw257.

68. Neph, S., Kuehn, M.S., Reynolds, A.P., Haugen, E., Thurman, R.E., Johnson, A.K., Rynes, E., Maurano, M.T., Vierstra, J., Thomas, S., et al. (2012). BEDOPS: high-performance genomic feature operations. Bioinformatics *28*, 1919–1920.

69. Trapnell, C., Pachter, L., and Salzberg, S.L. (2009). TopHat: discovering splice junctions with RNA-Seq. Bioinformatics *25*, 1105–1111.

70. Dobin, A., Davis, C.A., Schlesinger, F., Drenkow, J., Zaleski, C., Jha, S., Batut, P., Chaisson, M., and Gingeras, T.R. (2013). STAR: ultrafast universal RNA-seq aligner. Bioinformatics *29*, 15–21.

71. Bennett, M., Ulitsky, I., Alloza, I., Vandenbroeck, K., Miscianinov, V., Mahmoud, A.D., Ballantyne, M., Rodor, J., and Baker, A.H. (2021). Novel Transcript Discovery Expands the Repertoire of Pathologically-Associated, Long Non-Coding RNAs in Vascular Smooth Muscle Cells. Int. J. Mol. Sci. *22*, 1484.

72. He, Y., Selvaraju, S., Curtin, M.L., Jakob, C.G., Zhu, H., Comess, K.M., Shaw, B., The, J., Lima-Fernandes, E., Szewczyk, M.M., et al. (2017). The EED protein–protein interaction inhibitor A-395 inactivates the PRC2 complex. Nat. Chem. Biol. *13*, 389–395.

73. Atienza, J.M., Zhu, J., Wang, X., Xu, X., and Abassi, Y. (2005). Dynamic Monitoring of Cell Adhesion and Spreading on Microelectronic Sensor Arrays. J. Biomol. Screen *10*, 795–805.

74. Martello, A., Lauriola, A., Mellis, D., Parish, E., Dawson, J.C., Imrie, L., Vidmar, M., Gammoh, N., Mitić, T., Brittan, M., et al. (2020). Trichoplein binds PCM1 and controls endothelial cell function by regulating autophagy. EMBO Rep. *21*, e48192.

75. Fay, M.P., and Shaw, P.A. (2010). Exact and Asymptotic Weighted Logrank Tests for Interval Censored Data: The interval R Package. J. Stat. Software *36*, i02.

76. Huang, W., Loganantharaj, R., Schroeder, B., Fargo, D., and Li, L. (2013). PAVIS: a tool for Peak Annotation and Visualization. Bioinformatics *29*, 3097–3099.

77. Bardou, P., Mariette, J., Escudié, F., Djemiel, C., and Klopp, C. (2014). jvenn: an interactive Venn diagram viewer. BMC Bioinf. *15*, 293.

78. Mi, H., and Thomas, P. (2009). PANTHER pathway: an ontology-based pathway database coupled with data analysis tools. Methods Mol. Biol. *563*, 123–140.

79. Raudvere, U., Kolberg, L., Kuzmin, I., Arak, T., Adler, P., Peterson, H., and Vilo, J. (2019). g:Profiler: a web server for functional enrichment analysis and conversions of gene lists (2019 update). Nucleic Acids Res. *47*, W191–W198.

80. Chen, E.Y., Tan, C.M., Kou, Y., Duan, Q., Wang, Z., Meirelles, G.V., Clark, N.R., and Ma'ayan, A. (2013). Enrichr: interactive and collaborative HTML5 gene list enrichment analysis tool. BMC Bioinf. *14*, 128.

81. Kuleshov, M.V., Jones, M.R., Rouillard, A.D., Fernandez, N.F., Duan, Q., Wang, Z., Koplev, S., Jenkins, S.L., Jagodnik, K.M., Lachmann, A., et al. (2016). Enrichr: a comprehensive gene set enrichment analysis web server 2016 update. Nucleic Acids Res. *44*, W90–W97.

82. Herrero, J., Muffato, M., Beal, K., Fitzgerald, S., Gordon, L., Pignatelli, M., Vilella, A.J., Searle, S.M.J., Amode, R., Brent, S., et al. (2016). Ensembl comparative genomics resources. Database *2016*, bav096.

83. McLean, C.Y., Bristor, D., Hiller, M., Clarke, S.L., Schaar, B.T., Lowe, C.B., Wenger, A.M., and Bejerano, G. (2010). GREAT improves functional interpretation of cis-regulatory regions. Nat. Biotechnol. *28*, 495–501.

84. Huang, D.W., Sherman, B.T., and Lempicki, R.A. (2009). Systematic and integrative analysis of large gene lists using DAVID bioinformatics resources. Nat. Protoc. *4*, 44–57.

85. Davis, S., and Meltzer, P.S. (2007). GEOquery: a bridge between the Gene Expression Omnibus (GEO) and BioConductor. Bioinformatics *23*, 1846–1847.